SEMMELWEIS EGYETEM

DOKTORI ISKOLA

Ph.D. értekezések

3277.

SZIKLAI DOMINIK

Celluláris és molekuláris biofizika
című program

Programvezető: Dr. Kellermayer Miklós, egyetemi tanár
Témavezető: Dr. Kellermayer Miklós, egyetemi tanár

Topographical structure, nanomechanics and nanosurgical manipulation of biological supramolecular systems

PhD thesis

Dominik Sziklai

Theoretical and Translational Medicine Division
Semmelweis University

Supervisor:	Miklós Kellermayer, DSc
Official reviewers:	Gáspári Zoltán, DSc Kiss Levente, PhD
Head of the Complex Examination Committee:	Alán Alpár, DSc
Members of the Complex Examination Committee:	Mihály Kovács, DSc László Cervenák, PhD

Budapest
2025

Table of contents

List of abbreviations

ACE2	Angiotensin-converting enzyme 2
AFM	Atomic Force Microscopy
ATPase	Adenosine Triphosphatase
BSL	Biosafety Level
CoV	Coronavirus
DMEM	Dulbecco's Modified Eagle Medium
DMV	Double-Membrane Vesicles
DTT	Dithiothreitol
E	Envelope protein
EGTA	Ethylene Glycol-bis(β-aminoethyl ether)-N,N,N′,N′-Tetraacetic Acid
EH-myomesin	Embryonic Heart myomesin
ER	Endoplasmic Reticulum
ERGIC	ER-to-Golgi Intermediate Compartment
FBS	Fetal Bovine Serum
FJC	Freely Jointed Chain
GC	Gas Chromatography
HPLC	High Pressure Liquid Chromatography
M	Membrane protein
MERS	Middle East Respiratory Syndrome
MilliQ	ultrapure water produced by a Milli-Q water purification system from Millipore Corporation
N	Nucleocapsid protein
nsp	Non-Structural protein
OD	Optical Density
ORF	Open Reading Frame
PBS	Phosphate Buffered Saline
PEVK	domain of high proline (P), glutamate (E), valine (V), and lysine (K) content
RT-PCR	Reverse Transcription Polymerase Chain Reaction
S	Spike protein

SARS	Severe Acute Respiratory Syndrome
SDS	Sodium Dodecyl Sulfate
TWEEN 20	Polysorbate 20 (detergent)
VoC	Variant of Concern
VP-SFM	Virus Production Serum-Free Medium
WLC	Worm-Like Chain

1. Introduction

> *"I couldn't stop looking at the images. It was entering a new world."*
>
> *Gerd Binnig*

Biomolecular systems are constructed from a surprisingly small number of low-atomic-number elements. Yet, *via* their combination into polymers, a myriad of different molecules is built which can further associate into supramolecular systems of remarkable elegance, beauty and abilities. With the advent of special biophysical tools, such as the atomic force microscope (*AFM*), we have the ability to investigate not merely the structure, but also the internal associations and the mechanical features of these supramolecular biological systems. During my doctoral studies I had the unique opportunity to explore various biomolecular and supramolecular systems and gain special insights that allowed us to develop novel theoretical understanding. In the *Introduction* below I describe the biological systems investigated, the theoretical background and the experimental tools employed.

1.1. Supramolecular structures of biological systems

1.1.1. Architectural patterns of biological materials

Biological materials exhibit a highly organized and hierarchical structure, spanning from the molecular to the macroscopic scale (1). Within the hierarchy, the components exhibit modularity, where complex functions emerge from the assembly of simpler, repeating units. Symmetry, both in geometry and organization, contributes to stability and resilience, while asymmetry often introduces functional directionality (2). There is an intimate connection between structure and function: the architecture of biological materials is finely tuned through evolution to meet specific mechanical or biological needs, demonstrating a profound integration of form and purpose (3).

1.1.2. Supramolecular systems

The transition from single molecular structures to supramolecular assemblies on the mesoscale (**Figure 1a**) is a fundamental principle in biological organization (4), enabling complex functionality emerging from simple components. At the molecular level, proteins, nucleic acids, and lipids possess intrinsic structural motifs that drive self-assembly through non-covalent interactions such as electrostatics, hydrophobic effects, and hydrogen bonding (4). These interactions facilitate the formation of higher-order structures with specific spatial arrangements and emergent properties. For instance, cytoskeletal elements such as actin filaments and microtubules are formed by the polymerization of protein monomers into dynamic, modular networks that support cell shape and transport (5). In the nucleus, DNA wraps around histone proteins to form nucleosomes, which further fold into chromatin fibers, eventually condensing into chromosomes prior to cell division (5). Similarly, membrane systems arise from the self-assembly of amphiphilic lipid molecules into bilayers, which organize into intricate architectures such as the endoplasmic reticulum and the Golgi apparatus (5). These supramolecular structures embody the principle that function arises not just from individual molecules, but from their orchestrated arrangement in space and time. The described general structural principles weave and bind together all the supramolecular assemblies studied in this thesis.

1.1.3. General structure of proteins

Proteins are the fundamental structural and functional components of biological organisms, built from amino acids (**Figure 1b**). Protein structure is hierarchical: the primary structure is the linear amino acid sequence. The secondary structure—mainly *alpha* helices and beta sheets—is stabilized by hydrogen bonds. These fold into a tertiary structure, a 3-dimensional shape maintained by hydrophobic and polar interactions, ionic bonds, and disulfide bridges. Functionally distinct tertiary units are called domains. When multiple protein subunits assemble, they form a quaternary structure, a larger supramolecular complex (6).

Some proteins or regions, like the PEVK (high proline, glutamate, valine and lysine content) domain of the muscle protein *titin*, are intrinsically disordered, lacking a fixed 3-dimensional structure. In the case of *titin*, this region acts as an entropic spring, contributes to *titin*-actin interactions, and can change molecular rigidity in response to varying calcium levels (7).

1.1.4. The environment of proteins

Proteins exist in liquid environments composed mostly of water. Due to cytoplasmic crowding, anomalous diffusion and phase separations (8), the *in vivo* environment is usually very complex, so that no *in vitro* experiment in dilute solutions can imitate it completely. This poses a general limitation on most *in vitro* experiments, including the ones in this thesis.

From folding to stabilization, water molecules play a crucial role in the protein lifecycle. Moreover, proteins have a multilayer hydration shell around them (**Figure 1d**), and these water molecules can facilitate or hinder protein-protein interactions, or protein-surface interactions (9, 10). Generally, protein structural stability is heavily dependent on pH and ionic content of the solute and protein charge (11-13) (**Figure 1c**). When conducting AFM experiments, we must pay close attention and monitor the protein environment to acquire meaningful and consistent measurements.

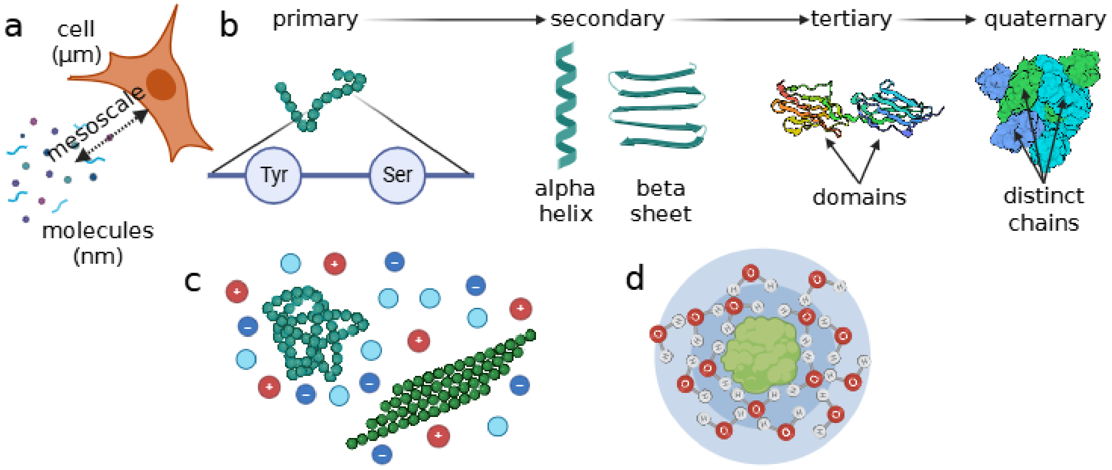

Figure 1. *General protein structure.* ***a)*** *Mesoscale is the place where the "atomic" and the "continuum" worlds meet. It encompasses structures from single molecules to supramolecular assemblies, generally not larger than a cell.* ***b)*** *The structural hierarchy of proteins.* ***c)*** *The dependence of protein structure on environmental factors. Some proteins take a globular form; others might aggregate or form oligomers under the same environmental circumstances, emphasizing the need to precisely tune protein environments for experiments.* ***d)*** *Proteins are surrounded by organized layers of water molecules, forming the hydration shell. This hydration shell enhances or hinders protein interactions and stabilization. (Created with BioRender.com)*

1.1.5. Adsorption and aggregation

Adsorption refers to the adhesion of molecules to surfaces, driven by the minimization of free energy through electrostatic and Van der Waals forces, hydrogen bonding, and entropy gain. It is influenced by both external factors (e.g., temperature, pH, ionic strength, surface composition) and internal, protein-specific factors (e.g., size, shape, charge, hydropathy) (14). Adsorbed proteins can also influence one another laterally, affecting conformation and packing. An important example for the ionic effect on adsorption in case of AFM is that potassium ions in the buffer can neutralize mica's (a frequently used surface in AFM experiments) negative charge, altering protein-surface interactions (14). Adsorption is critical to immobilize proteins in a controlled fashion. Therefore, calibrating adsorption under experimental conditions is essential to ensure reproducibility and meaningful interpretation of AFM measurements.

Protein aggregation occurs when proteins come into sustained contact, forming oligomers or larger aggregates (15). While often undesired in both biological and experimental contexts, aggregation can be functional when tightly regulated—for example, the self-assembly of muscle *myosin II* into thick filaments through tail-to-tail interactions, forming a bipolar structure crucial for muscle contraction. This process is regulated by ionic conditions, chaperones, and spatial constraints (16, 17).

1.2. Architecture of the muscle sarcomere

The sarcomere is the fundamental contractile unit of striated muscle tissue, serving as the smallest structural and functional module responsible for muscle contraction. It is a highly ordered, repeating assembly of protein filaments—primarily actin (thin filaments) and *myosin* (thick filaments)—arranged in a precise lattice that spans between two Z-discs (**Figure 2**). Giant *titin* molecules add further complexity to the sarcomere structure through their elastic nature and role in regularization. This intricate architecture enables the sliding filament mechanism, where interactions between actin and *myosin* drive the shortening of the sarcomere and, collectively, the contraction of muscle fibers. The sarcomere's regular, modular and oriented design exemplifies how biological systems translate molecular interactions into large-scale mechanical output (18).

1.2.1. Myosin thick filaments

The thick filament, also shown in **Figure 2**, is primarily composed of *myosin*, a motor protein with both enzymatic (ATPase) and structural functions. Skeletal muscle specific *myosin II* molecules form a bipolar array, with heads extending outward to interact with actin filaments during contraction (**Figure 2-inset1**). These heads hydrolyze ATP to generate the mechanical force needed for movement. The thick filament also includes associated proteins like *myosin* binding proteins C and H, which help regulate contractility and maintain filament structure (19).

1.2.2. The sarcomeric M-band: structure and biology

The M-band is a critical component within the sarcomere of striated muscles, it performs essential structural and signaling functions (20). It resides in the center of the sarcomere, intersecting thick filaments and linking them in a hexagonal array to stabilize the sarcomeric structure presented in **Figure 2**. The M-band plays a vital role in managing forces within the sarcomere, helping to mitigate mechanical stress and prevent misalignment of thick filaments during contractions (21).

The myomesin family (myomesin, M-protein/myomesin-2, and myomesin-3) serves as the primary structural linker within the M-band (22). *Titin*, the largest known protein, as already mentioned, spans from the Z-disc to the M-band (23). Within the M-band, *titin*'s C-terminal domains engage in cross-linking, reinforcing structural stability and contributing to elasticity by linking to both *myosin* and the myomesin proteins. Obscurin and obscurin-like 1 also contribute to the structural integrity and spatial arrangement of the M-band components (24), associating particularly with *titin* and myomesin (**Figure 2-inset2**) (25).

Variability in M-band composition, depending on muscle type, development stage, and species, allows for specific mechanical properties. For instance, M-protein is prevalent in fast-twitch and cardiac muscles, which are subject to higher contractile demands, while the presence of EH-myomesin (an elastic variant) in slow-twitch and embryonic heart muscles confers additional flexibility for eccentric contractions (when a muscle generates force while lengthening) (23).

Myomesin proteins function through an antiparallel dimerization at the M-band, linking the thick filaments symmetrically across the sarcomere's center (**Figure 2-inset2**). This dimerization provides elastic support, which is critical for maintaining structural stability under load. *Titin* and obscurin connect through Ig domains and large, possibly unstructured regions, further strengthening the M-band and supporting sarcomere function under repetitive contractile cycles (21, 23).

The M-band acts as a "shock absorber", dissipating mechanical forces across the sarcomere. This function is particularly vital for preventing the thick filaments from drifting during powerful or prolonged contractions, a process essential for the efficiency of muscle function. This stress absorption is supported by the elasticity of the M-band proteins, notably the modular extensibility provided by myomesin's unique structure (26, 27).

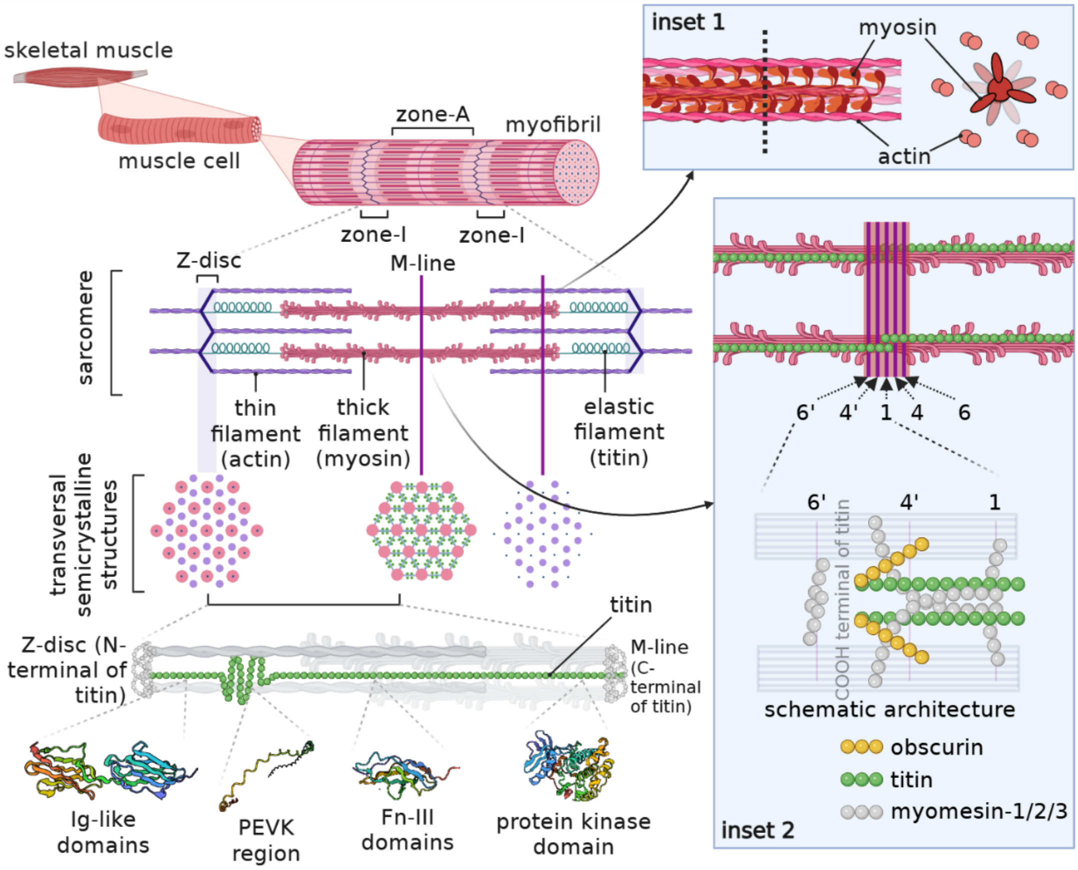

Figure 2. *Structure and molecular composition of the sarcomeric M-band. The nomenclature of the fine structure of muscle is rooted in EM and X-ray diffraction studies. From top to bottom, we can follow how a single muscle cell can be broken down into a repeating and well-organized structure, known as the sarcomere. The transversal sections illustrate how the thin and thick filaments overlap in the different regions of the sarcomere. At the bottom, I illustrate a half sarcomere with a highlighted titin indicating different domains.* ***inset1*** *presents the relative positions of thick (myosin) and thin (actin) filaments and shows how myosin head can interact with the actin filaments.* ***inset2*** *presents the structure of the M-line (on which my research concentrated) from a side-view. The numbering (6'-4'-1-4-6) follows the conventions of EM studies, the numbers denote the strongest five lines on EM images. These present molecular cross bridges inside the M-complex. (Created with BioRender.com)*

The M-band is also involved in signaling pathways essential for muscle adaptation. *Titin*'s kinase domain, located at the M-band periphery, interacts with various signaling proteins that transmit mechanical signals to the nucleus, affecting gene transcription related to muscle protein synthesis. Additionally, proteins involved in autophagy and protein turnover, such as Nbr1, p62, and MURF2, are localized in the M-band, linking the sarcomere's structural state to cellular metabolic pathways and proteostasis (28).

Mutations or deficiencies in M-band proteins, such as myomesin, *titin*, or obscurin, can lead to muscular diseases, including cardiomyopathies and muscular dystrophies. These pathologies often arise from compromised M-band integrity, which results in sarcomere instability and misregulated signaling pathways (29). The M-band's involvement in muscle disorders highlights its significance beyond mere structural support, emphasizing its role in cellular adaptation and response to physiological stress (30).

Titin and the thick filaments are closely linked in the sarcomere's structure and function. *Titin* spans from the Z-disk to the M-line, with a varying topological proximity and relative layout to the thick filaments. The question naturally arises: what interactions could be present between thick filaments (*myosin* molecules) and titin filaments? Titins within the M-zone lie on the surface of the thick filament shaft. In addition to the topological proximity, the superrepeat structure of titin coincides with the periodicity of the thick filaments (31), this provides a theoretical basis of their delicate interaction. But what is the result/function of this interaction? The most straightforward hypothesis is that titin might be a length controller of thick filaments, this theory is called the "titin-ruler", and several evidence of this was shown recently (31). If not a length controller, then titin might simply serve as a scaffold for the thick filament shafts, or a template for the formation of thick filaments. *Titin*'s primary roles may lie simply in stabilizing sarcomeric architecture and maintaining structural integrity during contraction, particularly through interactions at the Z-disk and M-line (32, 33).

1.3. Coronavirus

Viruses are high level supramolecular assemblies, as they contain proteins, lipids and genetic material in a very compact structural unit, called the virion. Coronaviruses are single-stranded RNA viruses with a genome size ranging between 25 and 32 kilobases, encoding structural and non-structural proteins. The beta-coronavirus genus includes severe pathogens such as SARS-CoV, MERS-CoV, and SARS-CoV-2, which have caused significant epidemic and pandemic outbreaks in humans (34). During my research, I studied SARS-CoV-2 (**Figure 3**).

Coronaviruses have spike (S) proteins on their surface, which play a critical role in cell entry by binding to host cell receptors. The binding to angiotensin-converting enzyme 2 (ACE2, which is not a receptor in a classical sense, but coronaviruses use it as receptors), combined with unique structural changes in the S-protein, allows SARS-CoV-2 to have a higher transmission efficiency compared to SARS-CoV and MERS-CoV (35). SARS-CoV-2 was first identified in late 2019 in Wuhan, China, and quickly spread globally due to its highly contagious nature.

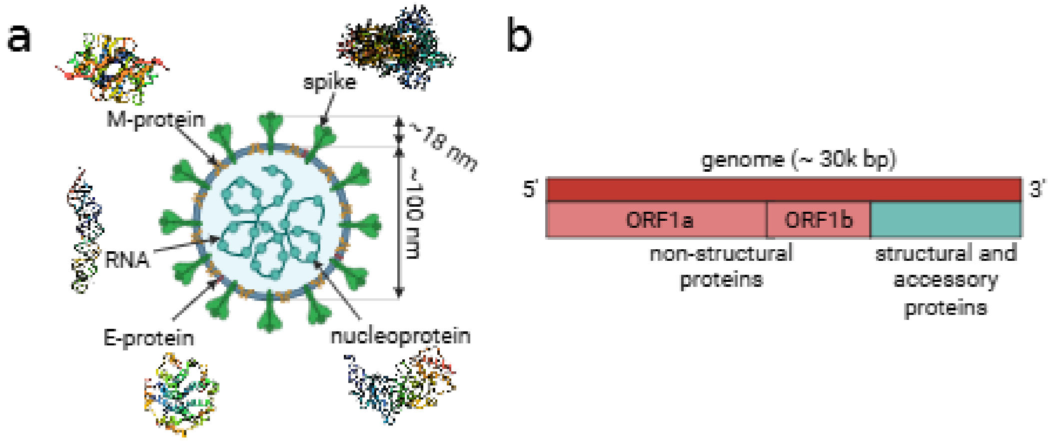

Figure 3. *Schematics of SARS-CoV-2.* ***a)*** *An illustration of the basic form of a coronavirus particle, with the structural proteins and genetic material highlighted. The approximate scales are indicated.* ***b)*** *The genome of SARS-CoV-2. (Edited with BioRender.com)*

While primarily a respiratory pathogen, SARS-CoV-2 can affect multiple organs, including the gastrointestinal, neurological, and cardiovascular systems (36). The virus is primarily transmitted *via* respiratory droplets and can also persist on surfaces and in the gastrointestinal tract, suggesting multiple infection routes (37).

1.3.1. Coronavirus virion structure

From a biological point of view, the role of a coronavirus particle is to protect and carry the viral genome, escape from the host cell and then enter another host cell (38). Every component of the virion serves this lifecycle. The proteins of the virion are encoded by the viral genome (**Figure 3b**). We distinguish two types of proteins: structural and nonstructural proteins (nsp). The structural proteins are the spike, the envelope (E), the membrane (M) and the nucleocapsid (N) proteins (**Figure 3a**). Nonstructural proteins are encoded in ORFs of the coronavirus genome (**Figure 3b**), and are responsible for tasks like RNA replication, cell membrane alteration and disruption of the host cell (39).

1.3.2. Variants

All viruses, including SARS-CoV-2, evolve over time, with most changes having little to no effect, while some mutations can impact transmissibility, disease severity, or the effectiveness of vaccines, treatments, and diagnostics (40, 41). Variants of SARS-CoV-2 have emerged with mutations mostly in the S-protein, some leading to increased transmissibility or immune evasion, notable variants include *alpha* and *delta* (42). The exact definition of a variant can be found in (43). In this thesis I refer to a variant as a variant of concern (*VOC*). *VOCs* can also be referenced as greek letters (that is why we use the "*alpha*" and "*delta*" naming). To clarify the parameters along which we can quantitatively differentiate between variants, I present a few terms (44):

- **Viral fitness:** reproductive success, the number of copies that a virus produces of itself normalized to e.g. a time interval. (analogous to the concept of general biological fitness)
- **Viral load:** the concentration of viral particles in a particular tissue or fluid.
- **Infectivity:** the capacity of the virus to enter the host cell and utilize its resources to replicate, leading to further infection.
- **Transmissibility:** how easily the virus moves from one individual to another (~ reproduction number).
- **Contagion:** communication of disease between host organisms, but including the environmental factors.
- **Severity:** seriousness of the symptoms.

1.3.3. Infection

Since the structure of coronavirus determines infection, I briefly provide a general overview of the infection mechanism. SARS-CoV-2 enters host cells either through membrane fusion, triggered by ACE2 receptor binding and protease cleavage (*e.g.* TMPRSS2), or through endocytosis. Inside the cell, the N protein dissociates from the viral RNA, which is then translated into polyproteins that are processed into nonstructural proteins (nsp1-16) to form replication and transcription complexes within double-membrane vesicles (DMVs) linked to the endoplasmic reticulum (ER). The newly synthesized viral RNA exits DMVs, structural proteins transit through the ER-to-Golgi intermediate compartment (ERGIC), and new virions assemble and bud into the lumen of the ERGIC before being released from the host cell (45).

1.3.4. Opportunity in coronavirus research

SARS-CoV-2 research has mainly focused on the S protein and its interaction with host receptors, given its major role in viral fitness (46). However, mutations in other structural and nonstructural proteins (nsp) also affect fitness, although they are less studied. These components may act synergistically, amplifying each other's effects.

While S–ACE2 interactions are easily studied through assays and simulations, such a narrow focus misses the full picture. The nanomechanical properties of the virion arise from the combined contributions of all proteins and the lipid envelope (47). It is known that structural differences of virion membranes affect the infection (48). Understanding these mechanics could reveal deeper insights into viral behavior and differences between variants.

1.3.5. Modelling a coronavirus particle

1.3.5.1. Vesicle

A coronavirus virion is surrounded by a lipid bilayer membrane vesicle. Lipids are fundamental to life, primarily serving to separate compartments, and they act as platforms for protein anchoring and reactions (49). The lipid membrane defines the shape of the virion, which in turn reveals key information about its geometry and mechanical properties. A membrane bilayer sheet has internal energy, and most of the modern approaches focus on the geometric contribution to internal energy—specifically, how small shape changes affect the membrane's energy landscape (50).

The geometry of such surfaces is best captured by using principal curvatures. These provide a coordinate- and parameterization-invariant way to describe surface shape (51). Below, I present the general formulation for the energy of an adhered vesicle (52-54):

$$F = -WA_{adh} + \oint \frac{1}{2} \kappa \, (c_1 + c_2)^2 \, dA \,, \tag{1}$$

where c_1 and c_2 are the two local principal curvatures [m^{-1}] of the membrane, κ [J] denotes the Helfrich bending constant (how resistant the membrane is against bending) (55), A_{adh} [m] is the contact area between the vesicle and the substrate, and W [Jm^{-2}] is the contact (adhesion) potential. dA denotes the area integral over the vesicle surface that is not in contact with the substrate, thus, the contact surface A_{adh} is not included within the integral.

The general model can be realized by using axisymmetric contours parameterized by the arc length s, with *Ψ(s)* being the tilt angle of the meridian curves (**Figure 4**).

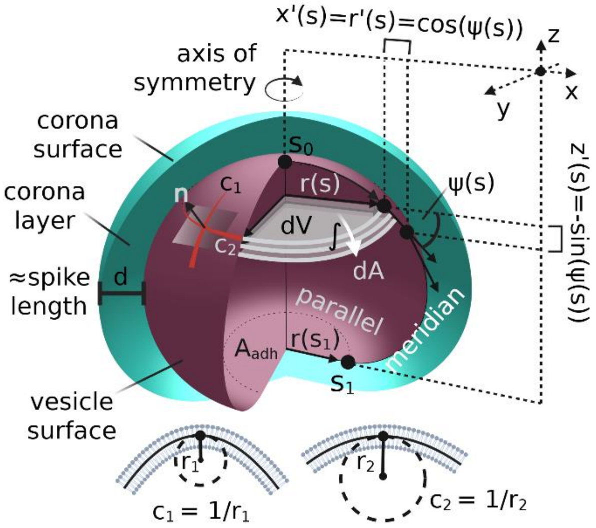

Figure 4. *Illustration of how the parameterized solution of the vesicle model results in the shape of the virion. The solution starts from* s_0 *along the profile curve (meridian) until reaches the substrate at* s_1*. The bottom gap is the adhered part of the vesicle (*A_{adh}*). For a surface of revolution, the principal curvatures are placed along the meridian and the parallel curves of the surface. The volume and force constraints are the infinitesimal volume and area elements (dV and dA). The curve parameterization is redundant, both r(s) and Ψ(s) can parameterize it individually, but calculations become easier when using both. Around the vesicle model, we define a shell that contains the S proteins. The 3D vesicle is easily formed by rotating the profile curve around the axis of symmetry (z-axis). (Edited with BioRender.com, adapted from (56))*

With our model defined, the problem of finding vesicle shapes becomes a problem of calculus of variations, where we wish to minimize the above energy functional. Moreover, to control the volume and area of the vesicle (constrained minimization), we further include two other parameters along with the above functional F (**Eq.1**):

$$F^* = F + \sigma A + PV. \qquad (2)$$

The two extra parameters in **Eq.2** are Lagrange multipliers: σ and P. σ [Jm^{-2}] is the multiplier for the area constraint, P [Jm^{-3}] is the multiplier for the volume constraint. A [m^2] is the vesicle surface and V [m^3] is the vesicle volume. An auxillary variable *r(s)* is also introduced to measure the distance to the revolution axis and ease the calculations. If we define *r'(s) = cos(Ψ(s))* and *z'(s) = -sin(Ψ(s))* (**Figure 4**), then c_1 becomes *Ψ'(s)* and c_2 becomes *sin(Ψ(s))/r(s)* as can be calculated from the first and second fundamental forms according to differential geometry. The principal directions of c_1 and c_2 are the meridians and parallels of the surface of revolution. After taking the first variation of *F**, the minimum (equilibrium) of the system yields a numerically solvable first order differential equation system (54).

The initial conditions were $r(s_0) = 0$, $\Psi(s_0) = 0$, $\gamma(s_0) = 0$ and $\Psi'(s_0)$ was varied as described later. The solution starts from s_0 until $\Psi(s)$ crosses π, this is where we reach the substrate. After numerically solving the system, we can render the curve (parameterized by s) back to the real shape of the vesicle in cartesian coordinates algorithmically.

Once having one meridian line (profile curve) of the vesicle surface, we generate the surface of revolution around the z axis (**Figure 4**, axis of symmetry) to render the vesicle in 3 dimensions. Thus, the vesicle becomes a closed surface of revolution. It is closed, because the bottom hole that remains after reaching s_1 is only a virtual hole, as the vesicle is closed there by A_{adh}.

In summary, this model enables numerical fitting of physically realistic vesicle shapes to our AFM measurement data (height and radius), incorporating bending rigidity (κ)—a key nanomechanical parameter reflecting membrane resistance to bending. The model excludes entropic effects and does not account for thermal fluctuations (see (57) for alternatives) and internal motions of the lipid envelope. Originally developed for giant vesicles, it may be less accurate for high-curvature systems like virions (50). However, its core principles could be refined by incorporating higher-order curvature terms (50).

1.3.5.2. Corona layer

The spike proteins are the most critical components of the virion during infection mediation. Anchored to the membrane, they behave as flexible, mobile probes (58-60) that bind host receptors. Though hard to resolve in AFM images (58), spikes were included in our geometric model due to their critical function. To represent them, we defined a corona layer around the vesicle (**Figure 4**), bounded by the vesicle surface and a translated corona surface. Each surface point x is extended outward along its normal $n(x)$ by a fixed distance d, so $x^* = x + d \times n(x)$. This creates a closed, convex surface that fully encloses the vesicle (**Figure 4**).

1.4. Atomic force microscopy

1.4.1. AFM overview

AFM is a powerful tool for studying biological samples at the molecular level. It uses a cantilever with a sharp tip to image structures at high resolution, revealing protein conformations, and the surfaces of cells, bacteria, viruses, and other biomolecular assemblies (**Figure 5a**) (61). Beyond imaging, AFM measures nanomechanical properties like elasticity and adhesion force, offering insight into mechanical stability and interactions at the piconewton scale (62). With the right modality and device, it can also track dynamic processes—such as protein folding or molecular binding—in real time under near-physiological conditions.

1.4.2. AFM experimental setup

The first step, proper sample preparation is essential for accurate and reliable AFM measurements. It enhances imaging stability and precision, allowing clear visualization of nanoscale features. Consistent protocols also ensure reproducibility and help confirm that observed phenomena stem from the sample itself, not preparation artifacts.

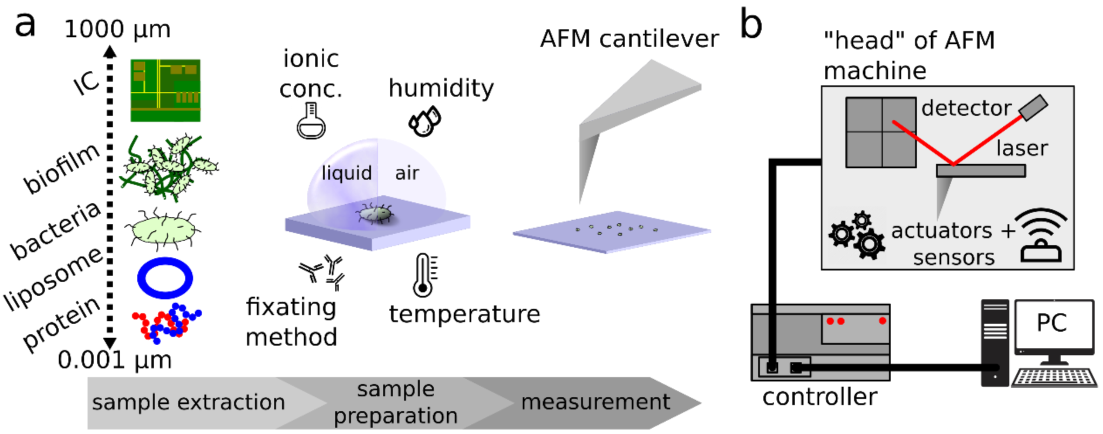

Figure 5. *Overview of AFM measurement and equipment.* ***a)*** *Basic AFM workflow, sample extraction and preparation are followed by measurement. Each step requires its own protocols and caveats to conduct biologically meaningful experiments.* ***b)*** *Schematic setup of an AFM, where the user controls and monitors the system mostly through the computer. The high-performance calculations for appropriate feedback are done by the controller module.*

AFM requires a stable surface to support the specimen during measurement (**Figure 5a**). This surface must be essentially atomically smooth and free of contaminants to prevent interference and ensure accurate interaction between the tip and the sample (63). In the experiments of this thesis, muscovite mica—an atomically smooth and flat crystal surface—was used unless otherwise specified (64).

The measurement medium also plays a critical role, especially for biological samples sensitive to environmental conditions (see **Introduction** and **Figure 5a**). A straightforward way is to do AFM measurements in gas (air) phase, although liquid media are often necessary to preserve native structure and function, as air exposure can cause dehydration or denaturation. Key parameters such as temperature and ionic composition must be controlled, as they influence mechanical properties and tip-sample interactions. Accurate regulation ensures biologically relevant results.

1.4.3. AFM technological overview

The key components of an AFM system include (**Figure 5b**) (62):

- **Cantilever:** A flexible beam with a sharp tip at its end.
- **Tip:** Usually made of silicon or silicon nitride, it interacts with the sample surface.
- **Laser and photodetector:** Used to detect the deflections of the cantilever.
- **Piezoelectric scanner:** Moves the sample or the cantilever in precise increments.
- **High performance electric controller:** Responsible for the integration, feedback and control of AFM components (sensors, actuators etc.) and data conversion and collection from devices. Moreover, it serves as a connection between the computer and the AFM hardware.

Since the advent of AFM, a myriad of operational modes was invented and implemented for specific use-cases. Here, I briefly introduce the three most frequently used operational modes of AFM and take a glimpse of their underlying physics (**Figure 6a-c**) (65):

1. **Contact mode**: The AFM tip maintains continuous contact with the sample surface. The cantilever deflection is directly related to the topography of the sample. This mode is governed by Hooke's law, $F=-kx$, where F is the force, k is the spring constant of the cantilever, and x is the cantilever deflection (**Figure 6b**).

2. **Dynamic mode (amplitude modulated):**
    a. **Tapping mode** (Intermittent Contact Mode): The cantilever oscillates slightly below its resonant frequency, and the tip intermittently contacts the sample surface. This reduces lateral forces and minimizes damage to soft samples. The oscillation amplitude, feedback and phase shift provide topographical and mechanical information (**Figure 6c**).
    b. **Non-contact mode**: The tip oscillates slightly above the resonant frequency, without making physical contact, sensing van der Waals forces. Changes in oscillation frequency or amplitude are used to map surface topography.

Since the tip radius of curvature is on the nanometer scale (**Figure 6a**), the arising tip-surface interactions can be approximated using the interatomic Lennard-Jones potentials (66). The derivative of the Lennard-Jones potential is the emerging force. This force can be attractive and repulsive. In **Figure 6b** and **c**, the force curves are shown.

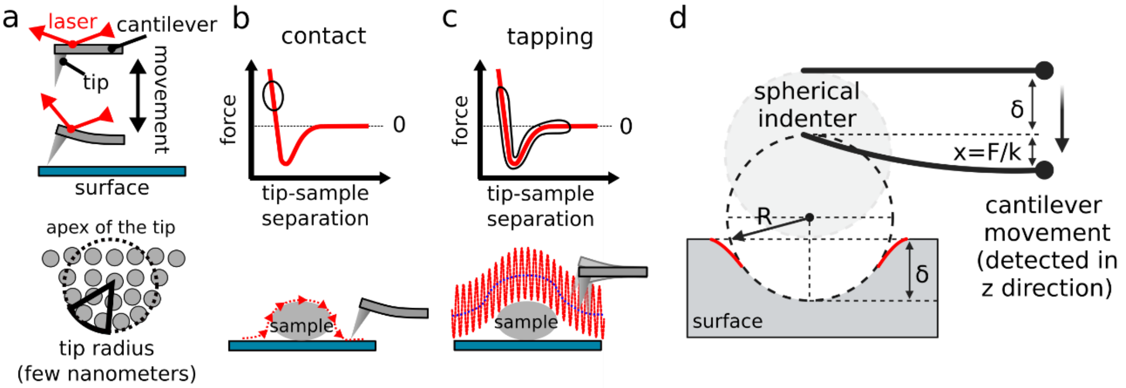

Figure 6. *AFM operating modes and surface indentation.* ***a)*** *The movement and bending of the tip (top). The end of the tip contains only a few molecules (usually* SiN_2*), resulting in a small effective tip radius (bottom).* ***b)*** *Force regime in contact mode and sample-cantilever relative positions.* ***c)*** *Force regime in tapping mode (amplitude modulation) and sample-cantilever relative positions.* ***d)*** *Geometry of the Hertz model for spherical indenter.* δ *is the indentation depth, which can be calculated by subtracting the deflection from the full distance traveled by the cantilever in the z direction (*$\delta = z - x$*). (Edited with BioRender.com)*

1.4.4. Contact mechanics of tip-surface interactions

When an AFM tip encounters the surface, there is a chance that it will indent that surface. One simple model for indentation is the Hertz model. The setup of the Hertz model (67) can be seen in **Figure 6d**. We have a sphere (a tip with a spherical end) that is pushed into the surface and begins gradual indentation as the sphere is pushed. The connection between the pushing force and indentation depth is $F \propto \delta^{\frac{3}{2}}$. This formula allows us to control the extent of indentation or avoid it entirely by monitoring the emerging forces.

1.4.5. Deconvolution of AFM images

In AFM, convolution refers to image distortion caused by the non-zero size and distinct shape of the probe tip, which broadens surface features (68)—especially when tip and sample have similar aspect ratios. As a result, sharp structures appear dilated or merged, limiting measurement accuracy for features near the tip's resolution.

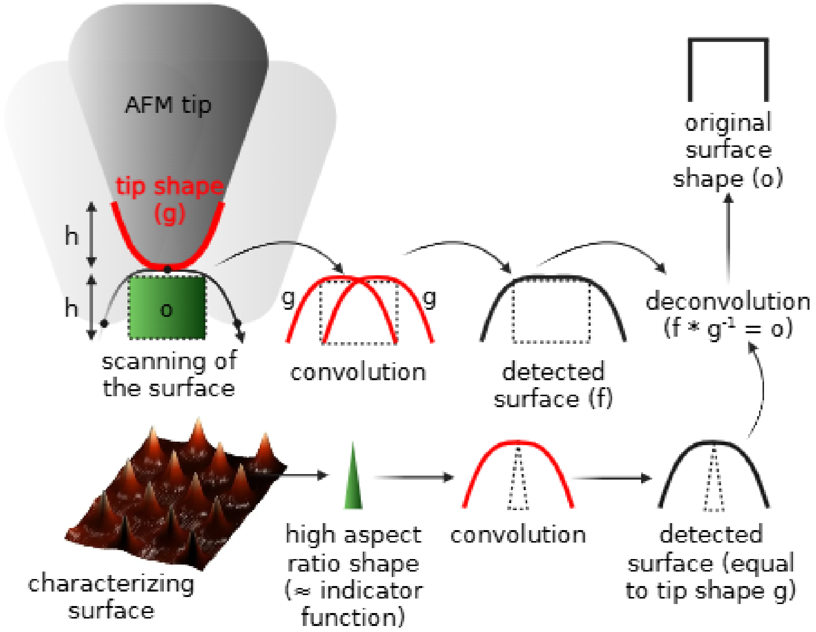

Figure 7. *The simplified theory behind topographical AFM image deconvolution. The characterizing surface helps identifying the shape of the tip. Using this shape, we can deconvolve the topographical image of the sample (h=height of o). (Edited with BioRender.com)*

Deconvolution, typically done *via* morphological erosion (69, 70), can partially correct for tip convolution if the tip shape is known or can be estimated. When the tip is unknown, blind reconstruction methods estimate its shape from the image alone. Morphological algorithms remain useful for both simulating and correcting AFM images. A simplified deconvolution methodology is shown in **Figure 7**.

1.4.6. An outline of modelling protein structures based on AFM topographical images

As discussed, AFM provides topographic images of surface-adsorbed molecules, capturing accurate height (z-axis) data with sub-nanometer precision, while width and length (x- and y-axes) are measured with slightly less accuracy (few nanometers). Information about internal structure is only indirectly accessible through amplitude and phase imaging (65). This limitation can be reduced by manipulating the objects on the surface, thus revealing the internal structure.

Most modeling in my research relies on basic geometrical and differential geometric principles, with some models incorporating linear elasticity theory (71). Given that molecules are surface-bound and typically much wider than tall, 2-dimensional models are often sufficient for accurate analysis. This section outlines the key modeling approaches used to interpret our experimental results.

1.4.6.1. Geometrical approach

Many folded proteins adopt filament-like forms, and these monomers often assemble into complex oligomers or polymers to perform higher-level biological functions (49). Their chain-like nature can be modeled using the freely jointed chain (*FJC*) model (72), which treats the protein as a series of rigid segments connected by frictionless joints. While simple and useful for estimating parameters like contour length, the FJC model overlooks steric effects and structural energy landscapes. A more realistic extension of the FJC model (73) is the worm-like chain (*WLC*) model (**Figure 8a,b**) (74). It accounts for intrinsic interactions along the protein filament: while segments are rigid over a given statistical length, flexibility increases with contour length. This statistical length is captured by a molecule-specific persistence length, which defines how far the molecule “remembers” its initial orientation. Proteins with globular tertiary structures, often formed through hydrophobic collapse (75, 76), can be approximated as ellipsoids. This simplifies comparisons of their width, length, and height in AFM analysis.

1.4.6.2. Linear elasticity

Linear elasticity, a branch of continuum mechanics, describes how solid, continuous bodies deform under applied forces (71). It assumes small, reversible (elastic) deformations and abstracts away atomic-scale details. Forces can be internal or external, applied at points, across surfaces, or throughout the body.

The core framework involves three types of equations: momentum (balance) equations, which describe how force is distributed (generalizing Newton's second law), strain-displacement equations, linking deformations to positional changes and constitutive equations, relating stress to strain through material properties (**Figure 8c**) (77).

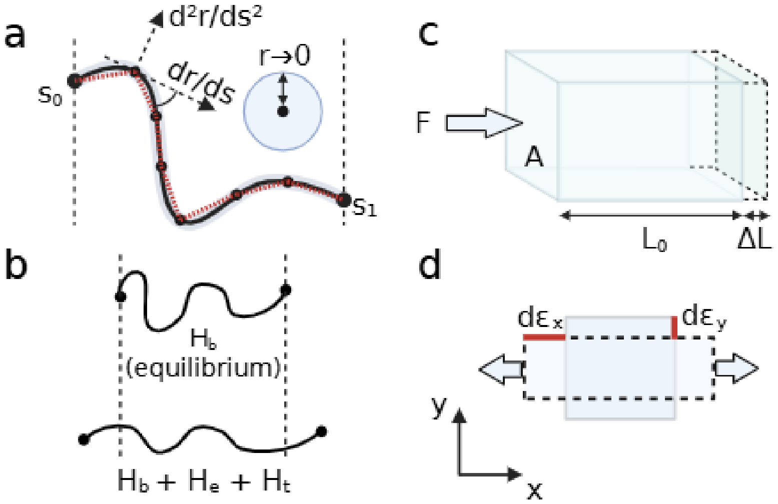

Figure 8. *Filamental models and the basics of linear elasticity.* ***a)*** *When modeling filaments in 2D, the filament radius is effectively reduced to zero, creating a midline curve. The red dashed segments are an FJC approximation of a molecule. The solid black line represents the WLC model for filamentous proteins. The intrinsic equilibrium shape is defined by the bending of the curve (curvature is the second derivative of the curve with respect to s, the parameter). This characteristic bending depends on the persistence length.* ***b)*** *If the filaments are not in their intrinsic equilibrium, we can extend the WLC to handle constraining energy components from elastic (H_e) and external (H_t) force effects.* ***c)*** *Graphical representation of stress = F/A and strain = $\Delta L/L_0$.* ***d)*** *Illustration of the Poisson's ratio in 2 dimensions. $v=-d\varepsilon_y/d\varepsilon_x$, essentially meaning that how the transverse strain (y) changed compared to the axial (x) strain. (Created with BioRender.com)*

Although the equations are complex, they are well-established for 2-dimensional geometries—suitable for AFM, where molecular height is much smaller than width. A key material parameter is Poisson's ratio (*v*), which quantifies how a material contracts perpendicularly when stretched (**Figure 8d**) (78). For biological materials, *v* is typically around 0.5.

1.4.6.3. Volume

Measuring molecular volume is challenging, as molecules lack sharp boundaries and volume estimates depend on the method used. We can use ensemble properties like molar volume (**Figure 9a**), calculated by dividing molar mass by density, and simulation-based estimates using electron cloud distributions (79). Another common approach to handle volume is the use of the Van der Waals volume (**Figure 9b**) (80, 81), which reflects the space occupied by a molecule based on the Van der Waals radii of its atoms. This volume, linked to repulsive intermolecular forces, can be derived from crystallographic data or the Van der Waals equation.

In AFM, the measured topography reflects the volume of molecules adsorbed to the surface, which - due to the imaging methodology - closely approximates the Van der Waals volume (82). The volume is derived pixelwise from raw imaging data (**Figure 9c**).

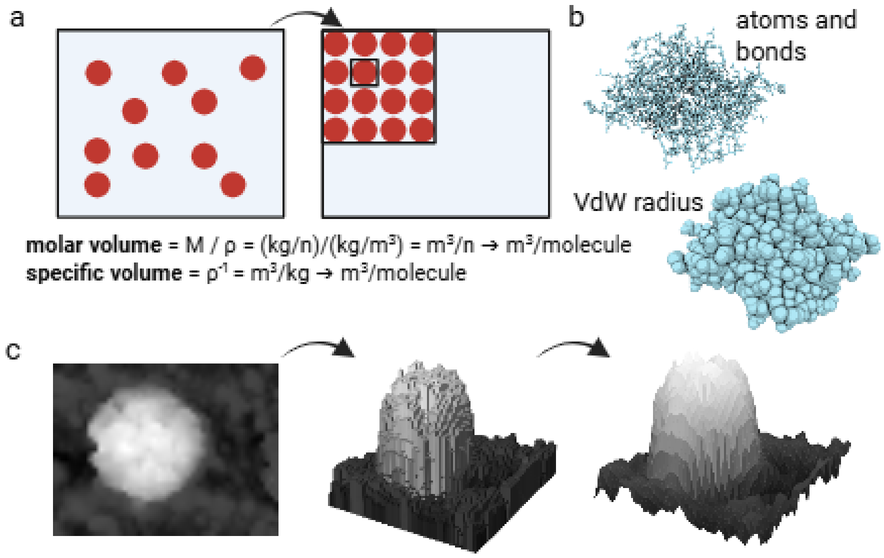

Figure 9. *Interpretation of molecular volume.* ***a)*** *Determining volume using statistical averages like molar or specific volume. (M = molecular weight)* ***b)*** *Interpretation of volume of single molecules, one practical approach is to use the Van-der-Waals radius.* ***c)*** *Volume approximation on AFM images. The 2-dimensional image is a height matrix (left), with volume = height × pixel area (middle). More precise volume information can be obtained by interpolation of the covering surface with triangulation (right). The AFM image shown was collected from a SARS-CoV-2 virion. (Edited with BioRender.com)*

1.5. Nanosurgery

As shown in **Figure 2**, the complex structure and function of the sarcomeric M-line make it difficult to study experimentally. While AFM studies on isolated components have provided insights, they offer limited information on the full supramolecular assembly (83-86). My research explored how AFM can be used to interpret and describe the large, M-band-derived *M-complex*. Although *in vivo* models of M-band structure and mechanics exist, AFM offers a complementary approach for resolving its molecular architecture. Biological systems are more than the sum of their parts, with numerous possible interactions (**Figure 10a**), making a holistic study of the M-band valuable—though technically challenging.

A key challenge is the inability to resolve individual molecular components within large complexes; AFM primarily captures the topography and response of the entire assembly. Working with bulky molecules complicates experimental design, particularly in defining the parameter space. Unlike single-molecule studies, which offer limited system-level insight and simpler parameter control, our *nanosurgery* method probes the mechanical behavior of the full molecular system.

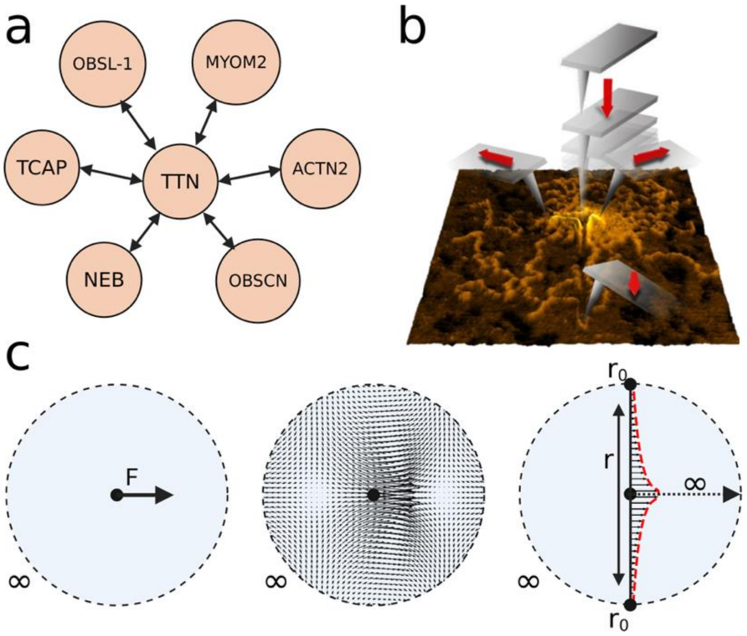

Figure 10. *AFM nanosurgery and bulk modelling.* ***a)*** *Part of the titin interactome (www.ebi.ac.uk) demonstrating the complex system that is hard to study through separated components.* ***b)*** *Graphical presentation of the nanosurgery method, first we push the AFM tip gently on the surface and then pull out in different directions to separate components.* ***c)*** *The 2D Kelvin problem. An in-plane force load is put into the infinite media (left). This force creates a displacement field (middle). Taking the displacement of the infinitesimal middle line ("filament") is an accurate model for the displacement of a filamental protein adhered to a surface. (Edited with BioRender.com)*

We named our method *nanosurgery* to reflect its mechanical mode of action (**Figure 10b**). With the AFM tip we disrupt and unfold protein structures directly on the surface, allowing us to probe the mechanical properties of complexes in a way that better reflects *in vivo* conditions than traditional single-molecule studies. *Nanosurgery* serves as a lateral-force counterpart to classical single-molecule force spectroscopy.

The method involves sequential steps: first, the AFM tip is lowered into the center of the surface-bound complex with minimal force to avoid indenting the surface and create debris. This pN-scale force is not sufficient to damage the mica due to its high (~GPa) Young's modulus (see Introduction, Contact mechanics part). The tip is then moved laterally under with parameters such as speed and direction varied to explore the mechanical response.

1.5.1. Models of mechanical disruption of proteins

During *nanosurgery,* we apply lateral forces, producing primarily 2-dimensional force vectors. The following models can be used to interpret the molecular topography resulting from these mechanical manipulations.

1.5.1.1. Filaments in bulk

The manipulation of surface-immobilized proteins can be approximated as a point force acting on a 2-dimensional bulk material. The resulting deformation (**Figure 10c**) can be described using continuum mechanics, specifically the Kelvin problem, which models stress and displacement from an in-plane point force in an infinite continuous medium (87-89).

Using a 2-dimensional bulk model for filamentous proteins is justified:

- It has been successfully applied in prior studies;
- Filamentous proteins can be approximated by their midline, and this midline can be treated as a filament embedded in a 2-dimensional bulk (**Figure 10c**, right);
- Surface adhesion mimics resistance from a bulk environment.

The resulting displacement field of the 2-dimensional Kelvin problem can be expressed as:

$$u_x(r) = \frac{(1+v)P_x}{4\pi E}(3-v)\ln\left(\frac{r_0}{r}\right) = constant\ \cdot \ln(\frac{r_0}{r}) \qquad (3)$$

P_x [N] is the force in the x direction, E [Pa] is the Young's modulus of the material, v is the Poisson's ratio. r_0 is the position along the filament where the detected displacement is 0, and r is the distance between the origin of the P_x force and the position along the filament (**Figure 10c**).

1.5.1.2. Force propagation

Force propagation through proteins during mechanical pulling is neither instantaneous nor uniform. Unlike idealized spring models, real proteins dissipate energy and respond dynamically. The distribution of force depends on protein structure, bond stability, and time-dependent processes such as bond rupture and environmental conditions (**Figure 11c**). When force is applied to one end of a polyprotein chain, tension travels along the molecule, typically unfolding domains in sequence (90, 91).

1.5.1.3. Protein fracture

When materials are deformed, they typically undergo elastic (reversible) deformation first, followed by plastic (irreversible) deformation, and eventually failure. Classical solid mechanics distinguishes ductile and brittle behavior based on how materials respond to stress (**Figure 11a**) (92).

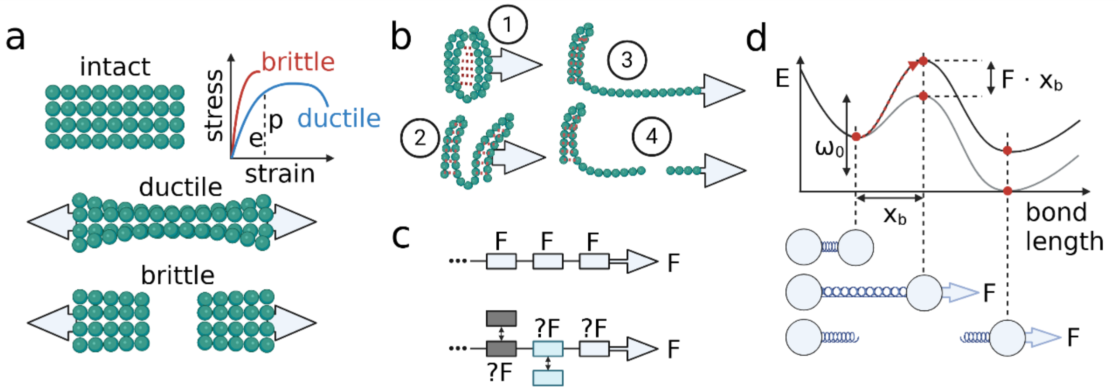

Figure 11. *Continuum and atomic models of protein fracture.* ***a)*** *Continuum behavior of materials and their stress-strain curves (p=plastic and e=elastic deformation). Ductile materials exhibit a marked deformation at the midplane with concentrated stress. This behavior causes the material to stay intact even after passing into the plastic (p) region of the curve. On the other hand, brittle materials are rigid, with a very steep and short elastic region, when they break, the deformation in the fractured region is minimal.* ***b)*** *Assumed naive hierarchical breaking of proteins. (see text for details).* ***c)*** *Force propagation for a simple, lossless series of springs (top), where the force distribution is uniform across the whole structure, for all springs. On the other hand, for a realistic protein (bottom) with multiple different domains and environmental interactions, the force distribution is heterogeneous.* ***d)*** *Illustration of the Bell model. The energy barrier for bond breaking is modified by the pulling force F, causing the natural vibration to jump over the barrier. (Created with BioRender.com)*

For biological protein materials like supramolecular complexes, mechanical failure is likely hierarchical, reflecting their structural organization. Intuitively, one expects disruption to proceed from quaternary to primary structure (**Figure 11/b**). In practice, the boundaries between structural levels blur, and environmental factors and internal crosstalk can redirect forces (**Figure 11/c**).

Generally, mechanical failure begins at the quaternary and tertiary levels, involving the disruption of non-covalent interactions. As stress increases, secondary structures—mainly stabilized by hydrogen bonds—are affected. Breaking the primary structure requires breaking covalent bonds between amino acids (along with occasional disulfide bridges), the strongest type of connection in the system (90, 92).

In larger complexes or bundles, spatial networks can distribute stress, complicating predictions. While AFM manipulation can reveal qualitative deformation through analysis of post-manipulation geometry, obtaining quantitative rupture data requires precise measurement of force, displacement, and probe velocity.

Here, I present a basic model of protein unfolding and bond rupture, the Bell model (**Figure 11d**). The model builds on the statistical nature of bond breaking. The base equation is the following (93, 94):

$$\chi = \omega_0 e^{-\frac{E_b - F x_b \cos\theta}{k_b T}}, \tag{4}$$

where ω_0 [s^{-1}] is the natural vibration frequency of a bond, E_b [J] is the energy barrier, F [N] is the pulling force x_b [m] is the distance between the minimum energy and the maximum energy (transition state). k_b [JK^{-1}] is the Boltzmann constant, and T [K] is temperature. Finally, we can deduce that χ [s^{-1}], the off-rate gives us the statistical time required for a bond to break due to the vibration frequency being able to jump out of the energy minima. The extended Bell theorem (92) defines the bond breaking speed as χ multiplied by x_b [ms^{-1}]. From this, we can derive that $F(v) \propto ln(v)$. So, the emerging force increases logarithmically with the pulling speed.

2. Research objectives

Generally, my research was the structural study and characterization of different nanomolecular structures. The experimental methodology that these projects shared was AFM. The specific goals were:

1. To explore the topographical structure of the synthetic *myosin II* thick filament and its interaction with *titin* and the M-band derived *M-complex*.
2. To investigate the topological structure of the sarcomeric *M-complex*
3. To dissect the *M-complex* with nanosurgical methods.
4. To uncover the topographical properties of *SARS-CoV-2* variants.
5. To model the elastic behavior of the *SARS-CoV-2* virion.

3. Methods

3.1. Preparation of the M-complex and single titin molecules

3.1.1. Isolation and purification

M-line complexes were isolated from the *m. longissimus dorsi* of male New Zealand white rabbits following established protocols (95-97) The experimental procedure received approval from the Semmelweis University Regional and Institutional Committee of Science and Research Ethics (approval number: XIV-I-001/29-7/2012) and the Directorate for Food-chain Safety and Animal Health of the Government of Pest County, in accordance with Hungarian legislation on animal protection and humane treatment (Law XXV*II*I/1998).

After homogeneization and centrifugation, the final purification step consisted of 1.5 mL of *titin*-rich supernatant (OD280 ~18), which was applied to a high-aspect-ratio Sepharose CL-2B (Sigma-Aldrich) column (length: 120 cm, diameter: 0.8 cm) (97). Elution was performed using a chromatography buffer composed of 30 mM K-phosphate (pH 7.0), 0.6 M KCl, 0.1 mM EGTA (Sigma-Aldrich, ≥98% complexometric), 0.3 mM DTT (Sigma-Aldrich, ≥98% HPLC), 2 µg/mL leupeptin (Sigma-Aldrich, ≥90% HPLC), 1 µM E64 (Sigma-Aldrich, ≥98% HPLC), 0.01% NaN_3 (Sigma-Aldrich, 99.0%), and 0.05% Tween-20 (>40% GC), at a flow rate of 0.2 mL/min. Fractions of 1 mL were collected during the elution process.

The samples were stored on ice in the presence of protease inhibitors (40 µg/mL leupeptin, 20 µM E64) and utilized within three weeks. The purity of the isolated *titin* was evaluated using vertical SDS agarose gel electrophoresis (0.8%), following standard protocols (98).

3.1.2. Sample preparation

Samples for AFM imaging were prepared following previously established protocols (97, 99). In brief, protein samples at concentrations ranging from 0.3 to 0.5 mg/mL were diluted 100-fold in chromatography buffer. Subsequently, 20 µL of the diluted solution was applied to freshly cleaved mica and incubated for 1 minute. The mica surface was then rinsed with MilliQ (Milli-Q Ultrapure and Pure Water Purification System) water and dried using high-purity N_2 gas.

In certain experiments, *titin* samples were subjected to meniscus forces using previously described methods (100). For this procedure, the protein sample was diluted in chromatography buffer supplemented with 50% glycerol. A 20 µL aliquot was deposited onto freshly cleaved mica mounted on a custom-built rotor, which was immediately spun at 13,000 rpm for 20 seconds. Following this, the sample was rinsed with MilliQ water and dried with N_2 gas. For imaging in liquid, the mica substrate with the sample was gently washed with 20% PBS, and AFM imaging was performed in this buffer.

3.2. Preparation of myosin thick filaments and co-precipitation with the M-complex

Myosin II was purified from rabbit *m. longissimus dorsi* following established protocols (101) using cycles of precipitation and dissolution at low and high ionic strengths (99). Monomeric *myosin* (∼30 mg/mL) was stored in 50% glycerol at −20 °C. Before use, glycerol was removed by either dialysis or another precipitation-dissolution cycle. Electrophoretic (and AFM) analysis confirmed the absence of *titin* contamination.

Thick filaments were prepared by diluting *myosin* into or dialyzing it against KCl-containing buffer (0–300 mM) as described by (102). For small volumes (<100 µL), dialysis was performed using a modified Eppendorf-tube cap with a dialysis membrane (Sigma-Aldrich, MWCO ~14k), against a 10,000× excess of buffer at 4 °C for at least one hour, or overnight (99). Samples were stored on ice and used within two days.

Titin and *myosin* were co-precipitated by dilution or dialysis into buffer (10 mM imidazole-HCl, pH 7.0, 2 mM $MgCl_2$, 0.05% Tween-20 (>40% GC)) containing 100–300 mM KCl (99). The protein ratio was set to match sarcomeric conditions (6 *titins*:150 *myosin*s per half thick filament; (103)). Concentrations were determined by OD_{280} using extinction coefficients of 1.0 mL/mg for *titin* and 0.53 mL/mg for *myosin*. Samples were kept on ice and used the same day.

3.3. AFM workflow

Nanosurgical manipulation was performed by applying the tip of an AFM cantilever onto the sample and then moving it laterally to displace specific regions of the *titin* molecular complex (97, 104). Initially, a control AFM image was captured using a Cypher ES scanner (Asylum Research, Santa Barbara, CA, USA) in tapping mode, with the setpoint adjusted to 60–70% of the cantilever's free oscillation amplitude to minimize the risk of unintended mechanical damage. Typical scanning rates ranged from 0.4 to 1.2 Hz. Silicon-nitride cantilevers (OMCL-AC160TS-R3, Olympus, Tokyo, Japan) were used, featuring a tip radius of 7 nm and a nominal spring constant of 27 N/m.

Following the initial imaging, parameters such as the starting point, direction, distance, and speed of AFM tip movement were set (97). The probe was then pressed against the surface in contact mode, applying a force between 150–600 nN. The speed and distance of tip movement varied between 10–1000 nm/s and 10–300 nm, respectively. After the nanosurgical manipulation, a second AFM image was acquired using the same scanning parameters as the initial scan to visualize structural changes induced by the procedure.

3.4. Preparation of coronavirus strains

3.4.1. Virus production

All virus preparation steps were performed under biosafety level 3 (BSL-3) conditions at the National Biosafety Laboratory, National Public Health Center, Budapest, Hungary. SARS-Cov-2 variants used in this study were: *wild type* (Wuhan-Hu-1), *alpha* variant (B.1.1.7) and *delta* variant (B.1.617.2) obtained from the Hungarian National Collection of Highly Pathogenic Viruses (56).

The variants were isolated from oropharyngeal swab of confirmed COVID-19 patients identified by RT-PCR. For virus production, we used monolayers of Vero E6 (European Collection of Authenticated Cell Culture, Salisbury, U.K.) cell cultures with approximately 75% confluence, cultured in DMEM (Sigma Aldrich) supplemented with 5% FBS (fetal bovine serum - EuroClone) and 1x Cell Culture Guard (PanReac AppliChem) in 5% CO2 environment (56).

The primary viral isolate was sequenced and propagated two times in cell cultures containing VP-SFM serum-free, ultra-low protein medium (Gibco) supplemented with L-glutamine (Sigma-Aldrich). Four days after inoculation the virus-containing medium was collected and centrifuged (3000 x g) to remove cellular debris. To concentrate the virus, the supernatant was ultracentrifuged (84,000 x g, 1.5 hours, 4°C) in 13.5-mL lockable plastic tubes using a Sorvall MTX-150 ultracentrifuge. The pellet was resuspended in 100 μL VP-SFM (56).

3.4.2. Substrate surface preparation

To stabilize the coronavirus particles on a smooth surface, we used an anti-spike antibody-functionalized surface (56, 58). These surfaces were prepared as described previously (58). Briefly, 100 µL of 10 µg/mL recombinant protein G was dropped onto the glutaraldehyde covered surface (Merck) and incubated for 30 minutes. The plate was then washed carefully five times with 100 µL phosphate-buffered saline (PBS). Then, 100 µL of 10 µg/mL SARS-CoV-2 Spike Glycoprotein Antibody (Abbexa Ltd) was placed onto the surface followed by 1 hour incubation. Lastly, the surface was washed with 100 µl PBS five times to remove the unbound antibodies. The antibody-coated surfaces were stored under PBS until application for up to 5 days at 4 °C.

3.4.3. Preparation of SARS-CoV-2 samples

An approximately 20 µL aliquot of purified SARS-CoV-2 sample was pipetted onto the pre-prepared anti-spike antibody-coated substrate surface and incubated at 37 °C for 25-30 minutes (56, 58). The process was repeated twice. Subsequently, we rinsed the surface with PBS to remove unbound virions. All the sample-loading and washing steps were carried out in a laminar-flow hood in BSL-3 conditions (at the National Biosafety Laboratory, National Public Health Centre, Hungary). For AFM imaging of chemically fixed SARS-CoV-2, 100 µL 5% GA solution (in PBS) was added, and the sample was incubated for approximately one and a half hour, ensuring both fixation and virus inactivation. Following these steps, the sample was carried to the AFM laboratory (Department of Biophysics and Radiation Biology, Semmelweis University) for loading in the environmental scanner unit of the Cypher ES AFM instrument.

3.4.4. AFM imaging of coronavirus

An Asylum Research Cypher ES instrument (Oxford Instruments, Santa Barbara, CA) was used for AFM imaging (56, 58). All measurements were performed at room temperature (25 °C). We used dynamic, amplitude modulated non-contact mode (AC) scanning utilizing BL-AC40TS (Olympus Corporation, Japan) cantilevers. The samples were under liquid, covered with ~100 µL PBS solution. The cantilever was oscillated near its resonance frequency (~20 kHz) by using photothermal or piezo excitation.

3.5. Coronavirus analysis

Particles were selected *via* Otsu thresholding. The resulting particle masks were manually refined, if needed. The final dataset consisted of 230 particles for the *wild type*, 130 for the *delta* variant, and 124 for the *alpha* variant (56).

We extracted the height for each particle from the center of the mask and average particle radius as presented in **Figure 14a,b**. Furthermore, we collected raw information like volume and surface area. We also calculated circularity (also known as isoperimetric quotient), which is a shape descriptor. It helps us quantify how close the shape of the mask of the given particle is to a perfect circle. It is calculated as the ratio of the area of the mask to the area of a circle having the same perimeter as the mask (105).

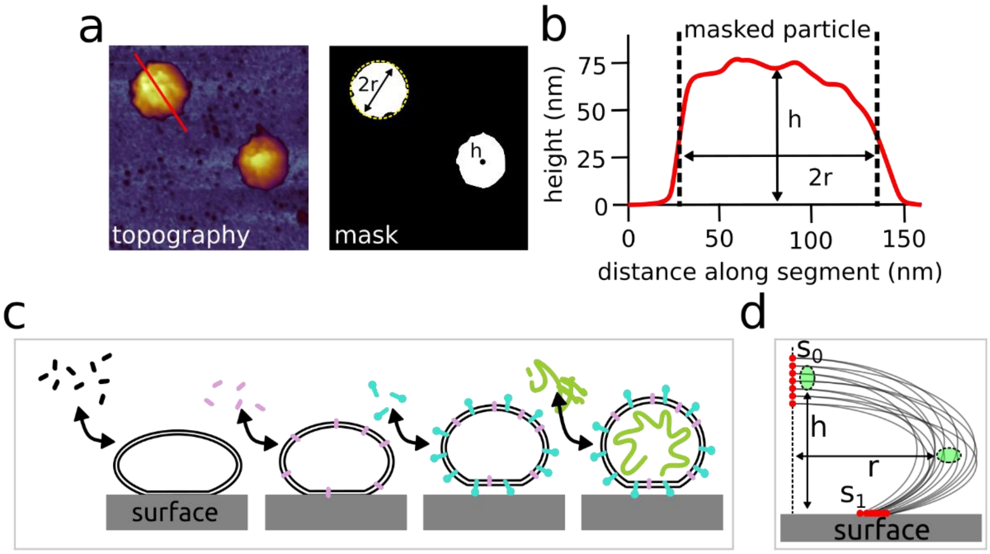

Figure 14. *Particle analysis and modelling theory.* ***a)*** *Masking of particles and measured parameters (r=radius, h=height).* ***b)*** *Topographical segment from* ***a)****.* ***c)*** *Theoretical construction (and deconstruction) of virions from its components.* ***d)*** *Shooting method for the boundary value problem, where the boundary conditions are the measured height and radius within error tolerance. Each curve starts from* s_0 *and ends in* s_1*. If a curve is contained in both green area, then it satisfies the boundary conditions and is accepted. (Adapted from (56))*

3.5.1. Fitting vesicle model to obtain geometrical data

AFM topography provides height per pixel values but does not resolve the contributions of individual layers. Based on our prior structural knowledge of coronavirus, the height of the virion on the surface is assumed to include a top spike layer, a vesicle core, and a bottom spike-receptor overlap (**Figure 15**). Due to variability in spike conformations (57) and bottom-layer overlap, exact height contributions are uncertain. The measurement of height at the particle center ensures consistency (**Figure 14a**).

To fit the vesicle model (**Figure 4**) to the virions, we solved the first order differential equation system described in the Introduction (53, 106). We required that $h_{virion} = h_{model}$ and $r_{virion} = r_{model}$. This is essentially a boundary-value problem. We can convert this boundary-value problem to an initial-value problem by using a shooting method, in which we slightly vary the initial values to find those parameter and initial value combinations which satisfy the boundary-value problem (**Figure 14d**). To increase robustness, we used the mean height and mean average radius per variant for model fitting (see **Table 3** in Results). Furthermore, a ±9 nm tolerance was introduced in all model fits to account for measurement uncertainty—roughly one-half of a spike's length (see **Figure 16-step1**).

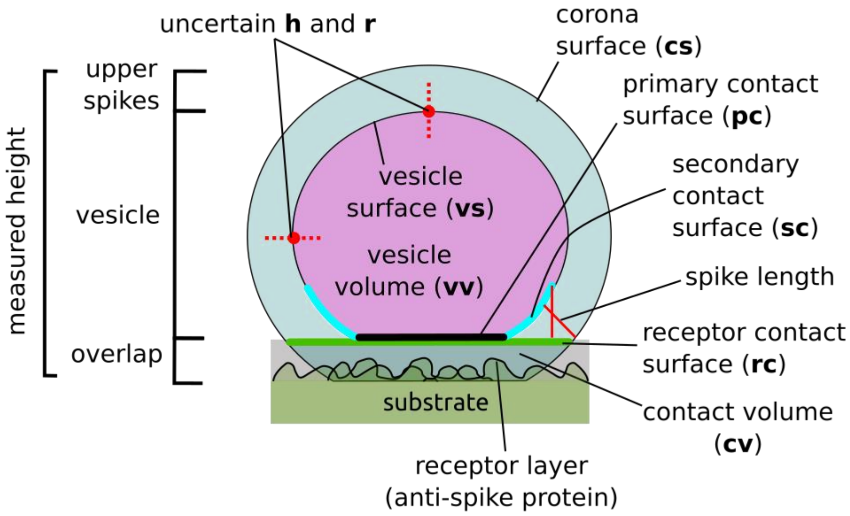

*Figure 15. Coronavirus geometry according to the AFM image. **a)** Illustration of the assumed geometrical layout of the virus on the surface. **b)** Analyzed finer geometrical properties of fitted models. (Adapted from (56))*

We then defined the corona layer as an 18 nm shell surrounding the vesicle (57, 107), created by translating each vesicle surface point outward along its normal (see **Figure 4**). This shell allows calculation of key geometrical parameters relevant to virus-host interaction, enabling comparison across variants (**Figure 15** and **Figure 16-step2**).

3.5.2. Estimating bending rigidity

To estimate bending rigidity (κ), we assumed that the virion can be abstracted into different components (**Figure 14c**), ultimately isolating the lipid envelope as a surface-bound liposome (56). We will use this abstract liposome to adjust its bending rigidity to transform its shape into the virion (**Figure 16**). Using a known fixed κ for liposomes (around 0.5×10^{-19} J (108)), we fit the vesicle model to generate the liposomes by adjusting Lagrangians of the area (σ), volume (P), and the initial slope condition $\Psi'(0)$ (**Figure 16-step3** left).

Next, fixing σ and P, we apply the shooting method (106, 109) (**Figure 14d**) to find the κ and $\Psi'(0)$ values that transform the liposome shape into that of the actual virion. The resulting κ provides an estimate of the virion's bending rigidity (**Figure 16-step4**).

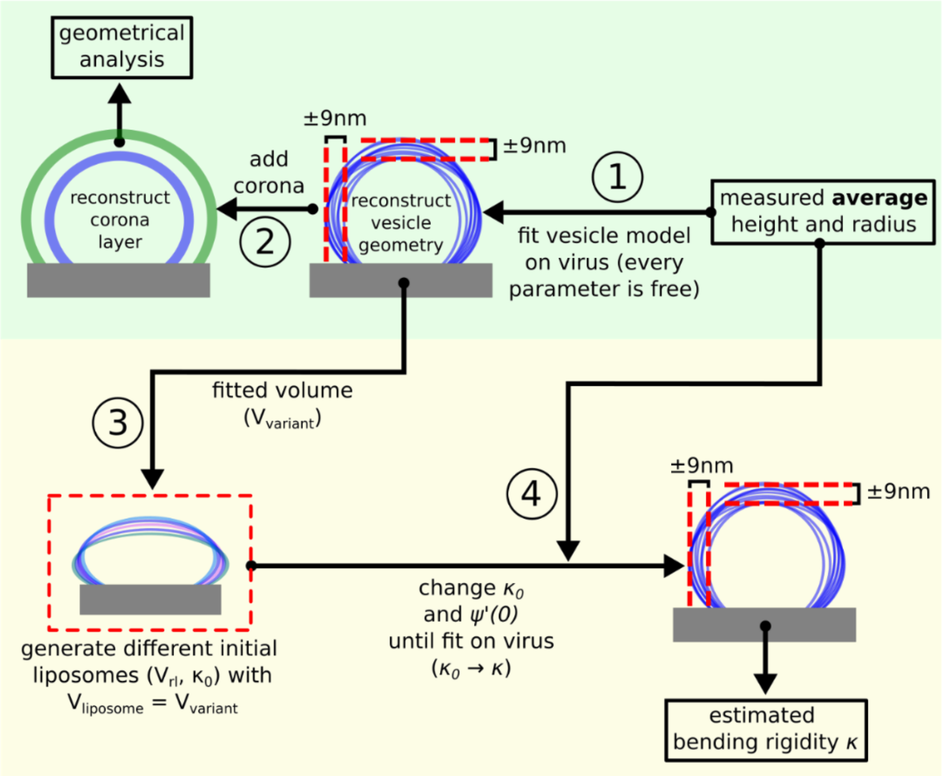

Figure 16. *Algorithm for geometry and bending rigidity estimation. (Adapted from (56))*

Several considerations apply to this method. First, we must define how the initial liposome resembles the virion. We choose volume equivalence ($V_{liposome} = V_{virion}$), meaning the model-fitted liposome shares the same volume as the virion whose bending rigidity is estimated. As a result, the liposome's surface area was ~5-10% larger than that of the virion. This increase in surface area can be theoretically justified by considering that when building the virion from the liposome, we exchange some lipids of the membrane to proteins. These proteins add curvature to the membrane (110).

Second, the estimated bending rigidity represents an apparent value, as it includes contributions from the membrane, embedded proteins, and internal contents. In the rest of the study, V_{rl} refers to reduced volumes of theoretical liposomes.

3.6. General image and data processing, numerical computations

Image post-processing and analysis were conducted semi-automatically using IgorPro (Wavemetrics, Lake Oswego, OR, USA) and Gwyddion (111). The process began with flattening the images to eliminate artificial distortions and ensure a planar background (112). Deconvolution was then performed using Gwyddion's built-in algorithm (70), incorporating the known shape of the AC-160 and the BL-AC40 cantilever tip for precise corrections.

Statistical analyses were carried out using Excel (Microsoft), Prism (Dotmatics) (113) and Python. For outlier removal we used Prism's ROUT method. Differential equation solutions, other numerical calculations and related data handling were implemented in Python, using the Numpy (114), Scipy (115) and Pandas (116) packages. For visualizations, we used the Matplotlib (117) and Seaborn (118) packages.

4. Results

4.1. Structure and mechanics of the thick-filament-M-complex system

4.1.1. Thick filament topography

AFM images of purified skeletal-muscle *myosin II* molecules revealed the typical two-headed structure, often with visible coiled-coil tails (99) (**Figure 17a**,**c**). Length measurements showed a narrow Gaussian distribution centered at 144.9 ± 14.6 nm, consistent with previous AFM and electron microscopy studies ~160 nm (119, 120).

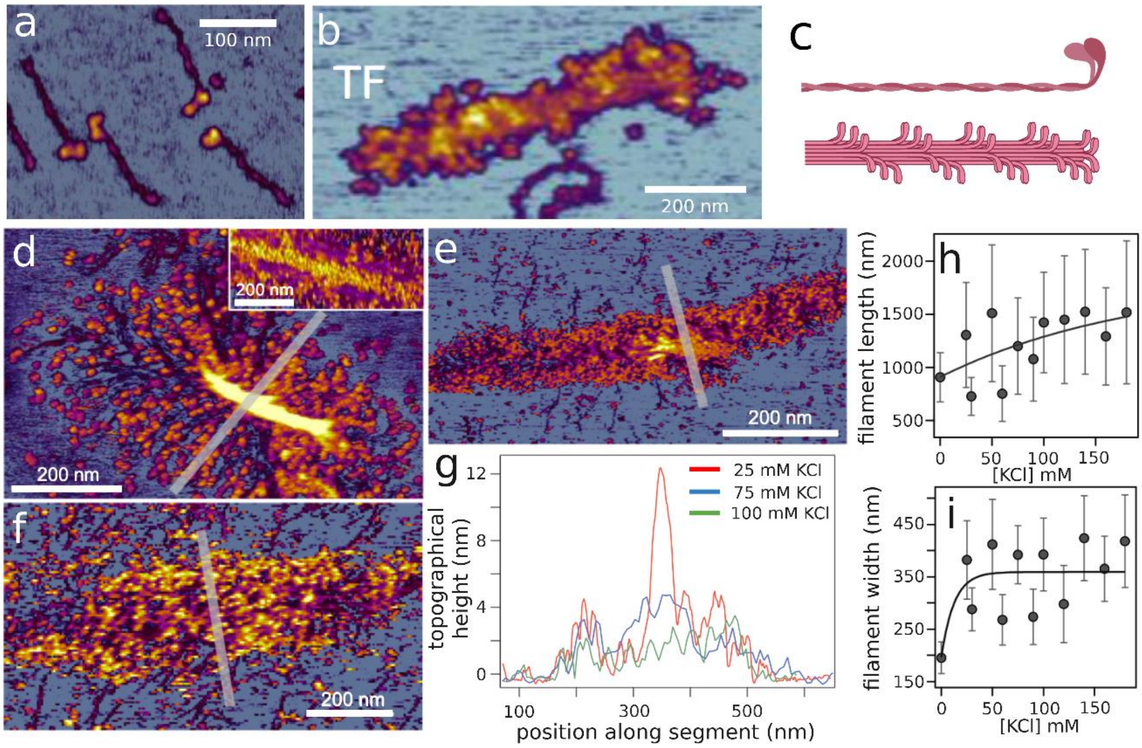

Figure 17. *AFM structure of the myosin thick filament.* ***a)*** *Double-headed myosin II molecules at low [KCl].* ***b)*** *Smaller myosin thick filament (TF).* ***c)*** *Schematic of the myosin II molecule and the thick filament.* ***d-f)*** *Thick filament with varying KCl concentrations, 25, 75 and 100 mM respectively, the topographical cross sections are shown on* ***g)****.* ***d) inset*** *shows a high-resolution image of the dense midline, revealing the myosin heads.* ***h)*** *and* ***i)*** *showing the saturating nature of both thick filament length and width. The fitted curves are exponential, but should only be interpreted as a guide for the eye (avg.±SD). (Adapted from (99))*

Reducing ionic strength induced thick filament formation, with structures displaying the characteristic bipolar shape and often a dense central core (**Figure 17b-g**) in the midline. High-resolution AFM images (**Figure 17d-inset**) showed that the core is a densely packed array of *myosin* heads. Filament length increased with KCl concentration (**Figure 17h**), saturating around ~1.5 μm above 100 mM KCl—similar to *in situ* sarcomeric dimensions. Filament lengths showed high variation, from 150 nm to 3.5 µm at 120 mM KCl . Apparent filament width also showed a saturating behavior above ~50 mM KCl (**Figure 17i**) and varied with ionic strength and between samples (**Figure 17d-g**).

4.1.2. Topographical structure, stability, and organization of the titin M-complex

The different fractions coming from the column chromatography (see 3.1.1. in Methods) contained several populations of molecules (**Figure 18a**). The first peak corresponds to M-line complexes, while the second peak contains *titin* monomers (97). A relaxed *titin* monomer is shown in **Figure 18b.iii**. Naturally, the *M-complex* structure appears on AFM images as a bulky, amorphous centre with long filaments reaching out of it in every direction (**Figure 18b.i**). The *titin* filaments interact in the central region with their C-termini.

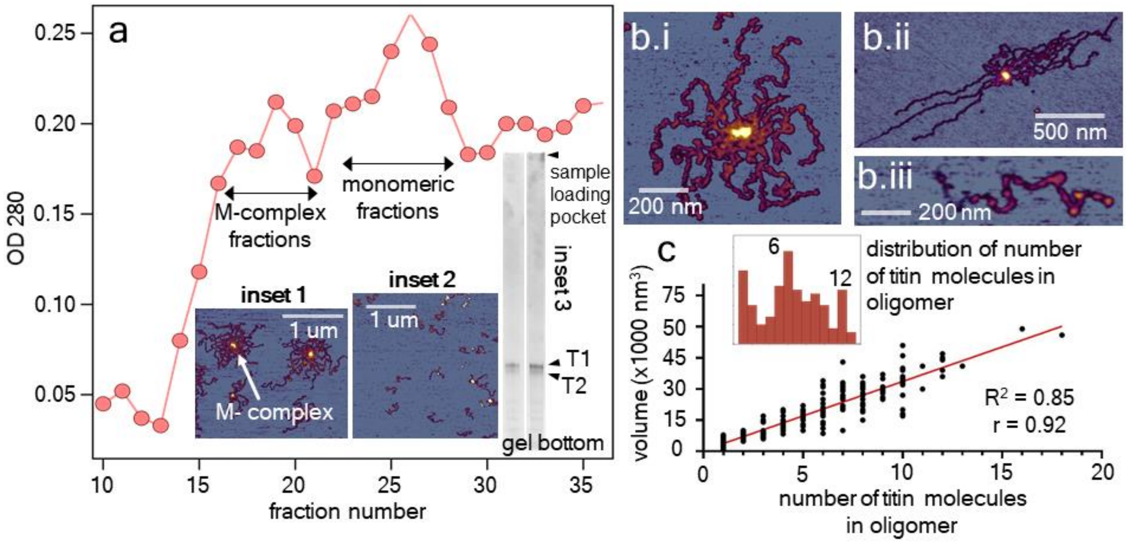

Figure 18. *AFM topography of titin and M-complex.* ***a)*** *The* OD_{280} *values of fractions during sample preparation, the two characteristic fractions are shown in inset 1 and 2. Inset 3. shows the SDS agarose (0.8%) gel profiles of purified titin samples. Left and right lanes are representative for M-complex and monomeric titin fractions, respectively.* ***b.i)*** *and* ***b.ii)*** *Topographical AFM images of titin oligomers (M-complexes) in relaxed and stretched state respectively.* ***b.iii)*** *A relaxed singular titin molecule.* ***c)*** *Volume of titin M-complexes as a function of number of titin molecules. The inset shows the distribution of the number of titin molecules in M-complexes. (Adapted from (97))*

As can be seen on the images, this central region can be idealized as a molecular hub, and this is what we reference as the sarcomeric *M-complex*. In several experiments, we used meniscus forces to stretch out *M-complex*es, this is illustrated in **Figure 18b.ii**.

The number of *titins* per *M-complex* varied (**Figure 18c**), and the histogram of *titin* distribution showed local modes at 6 and 12 *titin* molecules (99, 121) as indicated in the **Figure 18c-inset**. A strong linear correlation was found between *titin* count and *M-complex* volume (**Figure 18c**), with a zero intercept. *Titin* oligomers had shorter contour lengths than isolated molecules (*789 nm vs 453 nm*, (97)), indicating possible structural compaction near the *M-complex* from lateral strand interactions. We observed that the *M-complex* remained intact after treatment with 4 M urea, showing resistance to chaotropic agents and high ionic strength (97). However, the globular M-complex can still be digested by proteases (122).

4.1.3. Architecture of the M-complex

Large *M-complex*es sometimes displayed a thickened central region, suggesting condensed *titin-titin* interactions, possibly linked to their pairwise organization on *myosin* thick filaments (97, 123).

By analyzing the topography, some more delicate structures could be unveiled, likely corresponding to M-lines or the array structure of the M-band (21, 97, 124). In many large *M-complex*es, the marked central region appeared as a string or array of globular heads (**Figure 19a, b.i**), spaced at an average distance of ~30 nm (29.37 ± 7.12 nm, n = 20), as presented in **Figure 19b.i.profile**, **b.ii**. The observed variability in inter-complex spacing (~15–45 nm; **Figure 19b.ii**), may result from rupture of myomesin dimers between complexes, leading to rearrangements and uneven spacing (**Figure 19f**). Occasionally, broken *M-complex* arrays were seen (**Figure 19d**,**e**), supporting this explanation.

In some oligomers, the root of *titin* strands radiating into or out of the *M-complex* array were clearly visible (97) (**Figure 19c.i**), allowing measurement of *titin*-filament spacing (**Figure 19c.profile**). The mean spacing was 20.14 ± 7.12 nm (n = 14 in **Figure 19c.ii**), consistent with expected distances between *titin* quadruplexes in the M-band (21, 23, 125). The reconstruction of the *in situ* lattice based on our data can be seen in **Figure 19g**.

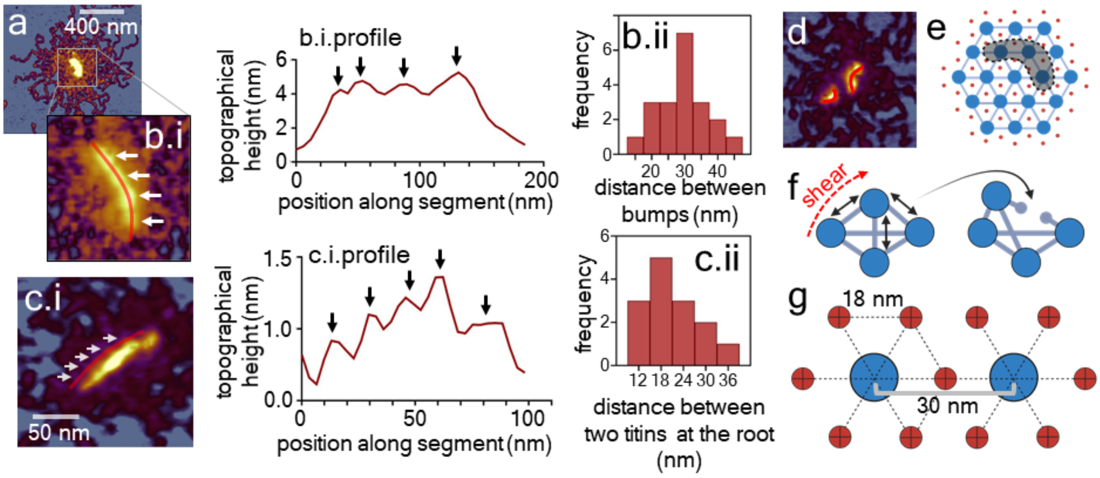

Figure 19. *Deducing the architecture of the M-line.* ***a)*** *A single M-complex.* ***b.i)*** *The finer structure reveals closely spaced bumps; a section of topography is showed on* ***b.profile****.* ***b.ii)*** *The distribution shows the inter-bump distances.* ***c.i)*** *The follow-up of titin molecules allows to measure the inter-titin distances at their roots.* ***c.i.profile)*** *A section of such a topography, and the* ***c.ii)*** *presents the inter-titin distance distribution.* ***d)*** *A presumably broken M-complex.* ***e)*** *An assumption on how our M-complex structures arise from the M-line array.* ***f)*** *We propose a simple explanation on why most M-complex breaks due to high mechanical stresses during the preparation of the sample.* ***g)*** *The reconstructed M-line array is formed by an almost perfect hexagonal structure and the scales are close to previously described values. (Adapted from (97))*

4.1.4. Thick-filament, titin and M-complex interactions

To explore possible *titin–myosin* interactions, AFM was used to image co-assemblies formed by direct dilution across decreasing ionic strengths (300–150 mM KCl) (99). At every KCl concentration, *titin* and *myosin* remained segregated with no structural evidence of binding (**Figure 20b**). To detect possible interactions more clearly, *titin* molecules were extended using the receding meniscus method (100). Across all tested KCl concentrations (150–300 mM), no specific *myosin–titin* binding was observed (**Figure 20a**). Occasional overlaps were indistinguishable from background and showed no binding pattern.

To assess whether structural equilibration enhances *titin–myosin* interaction, co-assemblies were formed by overnight dialysis at 100 mM KCl (99). This resulted in long, often interlinked thick filaments (**Figure 20c**), with compact *M-complex*es appearing as surface-bound bumps (**Figure 20c-inset**). These complexes differed from previously observed filament cores by their higher number, circular localization, and lack of distinct head structures.

Frequently, *titin* oligomers were located at or near thick-filament intersections, suggesting a potential role in suprafilamentous organization (99). In some cases, filament strands extended from oligomers along the filament axis, forming mesh-like surface structures (**Figure 20d**).

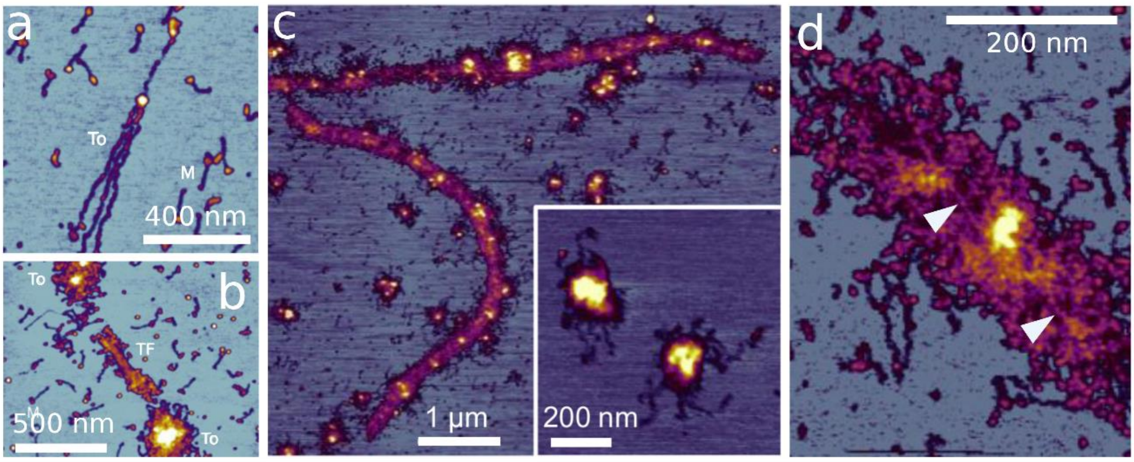

Figure 20. *Topography of the interaction between myosin and the titin M-complex.* ***a)*** *Appearance of stretched M-complex mixed with single myosin II molecules (To = M-complex, M = myosin).* ***b)*** *Possible interaction between M-complexes and myosin thick filaments (To = M-complex, TF = Thick filament).* ***c)*** *Result of slowly equilibrated thick-filament and M-complex mixtures. The inset shows the individual M-complexes.* ***d)*** *A close-up topographical image showing how the outreaching titins run along the thick filament in each direction (arrows showing titin molecules on the thick filament). (Adapted from (99))*

4.1.5. Nanosurgical manipulation of titin molecules

We initiated nanosurgical perpendicular manipulation by targeting *titin* filaments extending into or out of the *M-complex* (97). No specific titin region was targeted, the only criteria were that it should lie perpendicular to the direction of the cut. Since most of the titin domains are Ig-like and Fn type-III, it is very possible that we encountered such domains during nanosurgery. First, we tested how manipulation speed affects filament behavior. At a low AFM tip speed (10 nm/s in **Figure 21a.i, a.ii**, **b.i**), *titin* filaments displaced perpendicular to their orientation were stretched and eventually ruptured at their distal ends (**Figure 21a.ii**). Height profile analysis showed a reduction in filament diameter from ~0.3 nm to ~0.2 nm (**Figure 21a.i.profile**, **a.ii.profile**).

At a higher tip speed (1000 nm/s), similar deformation occurred (**Figure 21b.ii**), but with quantitative differences (97). At 10 nm/s, the manipulated segment showed a relative extension, calculated as $(L_1 + L_2)/L_0$, of ~4 (**Figure 21b.i**); at 1000 nm/s, the strain increased to ~6 (**Figure 21b.ii**).

At high speed, only a short *titin* segment detaches, presumably as the surface bonds can't dissociate quickly enough (97). However, the resulting strain is high due to the rapid buildup of intramolecular stress. In contrast, at low speed, a longer *titin* segment is progressively dislodged, allowing stress and strain to distribute over a greater length, resulting in lower overall strain. Despite these differences, the final lengths of extended segments were similar, averaging ~65 nm (65.61 ± 18.97 nm, n = 28).

Complete rupture was difficult to confirm, as fully unfolded domains lack sufficient contrast in AFM images (97, 100). Given that a *titin* domain spans ~4 nm (126), with unfolding steps of ~28 nm (127), the 6-fold extension observed at 1000 nm/s (**Figure 21b.ii**) likely corresponds to full unfolding of a ~5-domain segment.

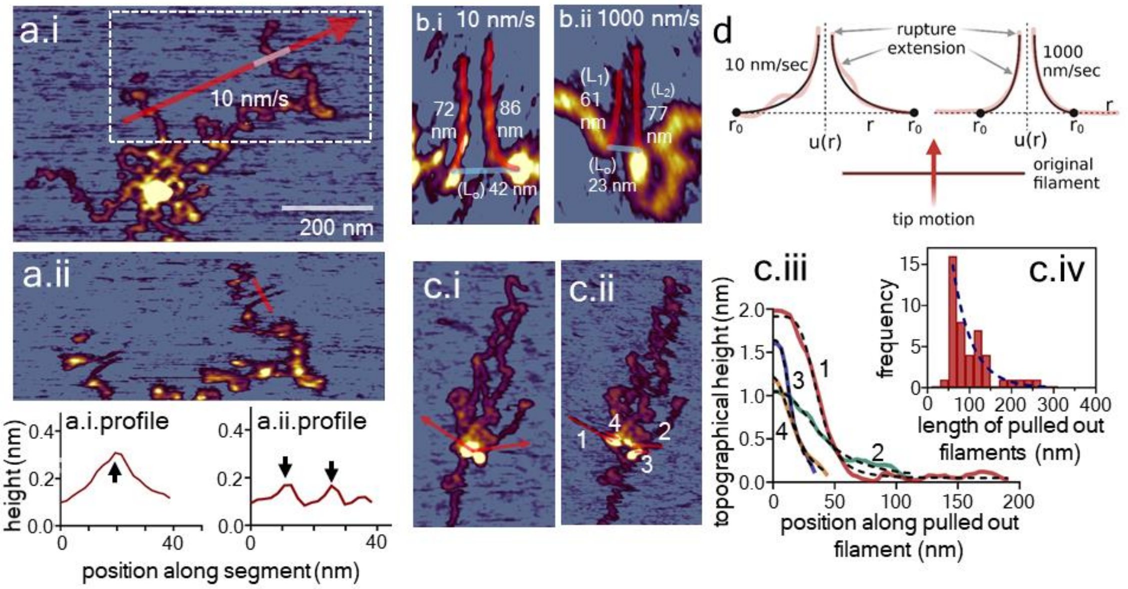

Figure 21. *Nanosurgery of titin molecules.* ***a.i)*** *and* ***a.ii)*** *Cutting through single titin molecules perpendicularly. The topography of the red segments is shown on* ***a.i.profile*** *and* ***a.ii.profile****, before and after respectively.* ***b.i)*** *and* ***b.ii)*** *shows the fitted curve (Kelvin solution) on the cut molecules.* L_1 *and* L_2 *is the length of the extended filaments on each side (red), while* L_0 *is the original, intact filament length (light blue).* ***c.i)*** *and* ***c.ii)*** *presents the before and after topography of a pre-stretched and manipulated M-complex. The topography of the numbered pulled-out filaments can be seen on* ***c.iii)****. The distribution of the pulled out filament lengths are shown on* ***c.iv)****.* ***d)*** *Fitting the modified Kelvin solution onto the manipulated filaments. (Adapted from (97))*

We carried out a least-squares fit to the raw data obtained by superimposing a *u(r)* (from the Kelvin solution, see in Introduction) versus *r* coordinate system on the AFM image of the nanosurgically manipulated *titin* loop (97) (**Figure 21d**). The original model fails to provide an optimal fit due to the formation of an emphasized gap between the strands at the vertex of the molecular loop, which is caused by the AFM tip itself (**Figure 21b.i,**

b.ii). By incorporating the AFM tip radius as a shift factor *d* into the model, we obtain a new set of equations:

$$u(r) = \begin{cases} k \cdot ln\left(\frac{-r_0}{r+d}\right), & r < 0 \\ k \cdot ln\left(\frac{r_0}{r+d}\right), & r > 0 \end{cases}, \tag{6}$$

which provide a significantly better fit to our nanosurgical manipulation results.

4.1.6. Nanosurgical manipulation of the titin M-complex

We performed nanosurgical manipulation of the *titin M-complex* at varying levels of complexity (97). First, we tested the effect of cutting through the *M-complex* center using AFM tip speeds of 10 and 1000 nm/s. Slower speeds resulted in more thorough cuts, likely because the slower rate allowed sufficient time for disrupting molecular interactions that hold the complex together. High-speed cuts dislodged only small regions, prompting the use of 10 nm/s tip speeds in later experiments for more effective manipulation.

To standardize the manipulation process, we always used 2-3 perpendicular tip movements from the same starting point in the *M-complex* center (97). Despite debris interference, filament loops could be pulled out in multiple directions, suggesting the *M-complex* contains a reservoir of filaments. To improve visibility, we pre-stretched *titin* oligomers using meniscus forces, aligning filaments with the centrifugal force direction (**Figure 21c.i, c.ii**).

Subsequent manipulations revealed distinct pulled-out strands (97) (**Figure 21c.ii**). The topographical height of these strands decayed with distance from the *M-complex* center and fit a sigmoidal function (**Figure 21c.iii**), indicating a transition from a dense core to thinner extensions. Filaments as long as 300 nm were extracted (**Figure 21c.iii, c.iv**), and their length distribution showed exponential decay, consistent with the sigmoidal height profile. The sigmoid function has the form:

$$B + \frac{(T-B)}{\left[1+\left(\frac{half\ height}{x}\right)^{S}\right]}, \tag{7}$$

where *B* and *T* are the minimal the maximal heights, respectively, *half height* is the distance where topographical height equals *(T − B)/2*, and *S* is a slope factor related to the steepness of the curve.

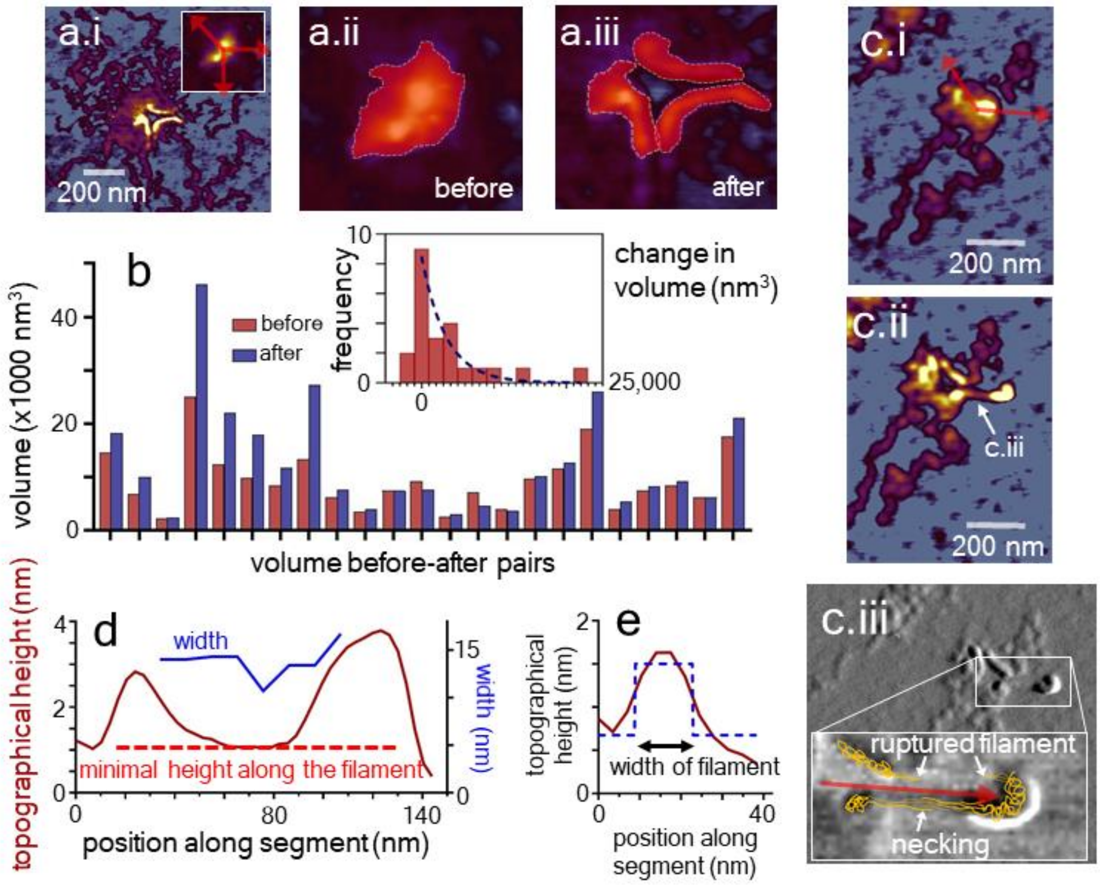

Figure 22. Nanosurgery of the M-complex. ***a.i)*** *The topography of the M-complex before manipulation (inset shows the directions of manipulation).* ***a.ii)*** *and* ***a.iii)*** *Masked areas for which the before and after volumes were calculated.* ***b)*** *Before and after volumes (inset show the distribution of the volume changes).* ***c.i)*** *and* ***c.ii)*** *shows the before and after topography of an M-complex.* ***c.iii)*** *shows the amplitude image (for better details) of the final state. The inset zooms on the region where we notice a so-called necking, a behavior mostly present in ductile materials.* ***d)*** *The topography along the necking region showing height and width.* ***e)*** *The method how the width was calculated in* ***d)****. (Adapted from (97))*

We measured volume changes in the *titin M-complex* induced by nanosurgical manipulation (97) (**Figure 22a,c**). Volumes before and after manipulation were quantified by image thresholding and segmentation (**Figure 22a.i, a.ii, a.iii**), with pairwise comparisons shown in **Figure 22/b**. Most manipulations resulted in increased *M-complex* volume, with the distribution of volume increments displaying an exponential trend (**Figure 22b-inset**).

When manipulating bulkier *M-complex* structures (like in **Figure 22c.i**, **c.ii**), such as *M-complex* arrays, we observed necking, characterized by localized thinning of the pulled-out filament (97) (**Figure 22c.iii**). In these cases, part of the *M-complex* array was displaced and pushed away from the manipulation site. The connecting filament between the displaced and stationary segments became stretched and showed reduced height at the midpoint (**Figure 22d,e**), indicating plastic deformation.

4.2. Coronavirus geometry

4.2.1. Topographical analysis

Representative AFM images of variants are shown in **Figure 23a**. AFM measurements revealed that the geometrical parameters of SARS-CoV-2 variants show considerable differences (56) (**Figure 23b-d**, **Table 1**).

Table 1*. Basic topographical measurements of coronavirus virions. Data are shown as mean±SD. The definition of circularity is given in the Methods. (56)*

variant	**mean of average radii** (nm)	**mean height** (nm)	**volume** ($x10^6$ nm^3)	**circularity**
wild type	65 ± 10	100 ± 15	0.85 ± 0.30	0.85 ± 0.06
alpha	59 ± 8	61 ± 12	0.46 ± 0.13	0.87 ± 0.06
delta	56 ± 7	83 ± 11	0.48 ± 0.12	0.86 ± 0.05

The *alpha* variant had the lowest and the *wild type* the greatest topographical height, while the height of *delta* particles lied in between (56). The volume distribution of the *wild type* coronavirus had the greatest standard deviation (SD) compared with the other two variants, and it had an overall greater mean than the other ones. The *wild type* had the greatest radius. The circularity of the three variants were very close for all three variants. **Figure 23b-d** show the height, mean radius and volume distributions of the measured data. We analyzed the linear correlations between measured variables to gain insights and quantify their possible connection (**Table 2**).

While **Figure 23e** shows essentially no correlations between the mean radius and the height, we found pronounced correlations between mean radius and volume, and notably these correlations are slightly different for each variant (56) (**Figure 23f**). The schematics in **Figure 23g** show the suggested mechanism underlying these correlations: as the radius of the variants changed, their height stayed relatively constant. We calculated how the volumes should change as a function of radius for such 3D geometries presented in **Figure 23g** and found that our measurement data almost perfectly follow such a relationship (colored dotted curves present this expected relationship on **Figure 23f**). For comparison, the dashed black line in **Figure 23f** indicates what the expected volumes should be for perfect spheres as a function of radius.

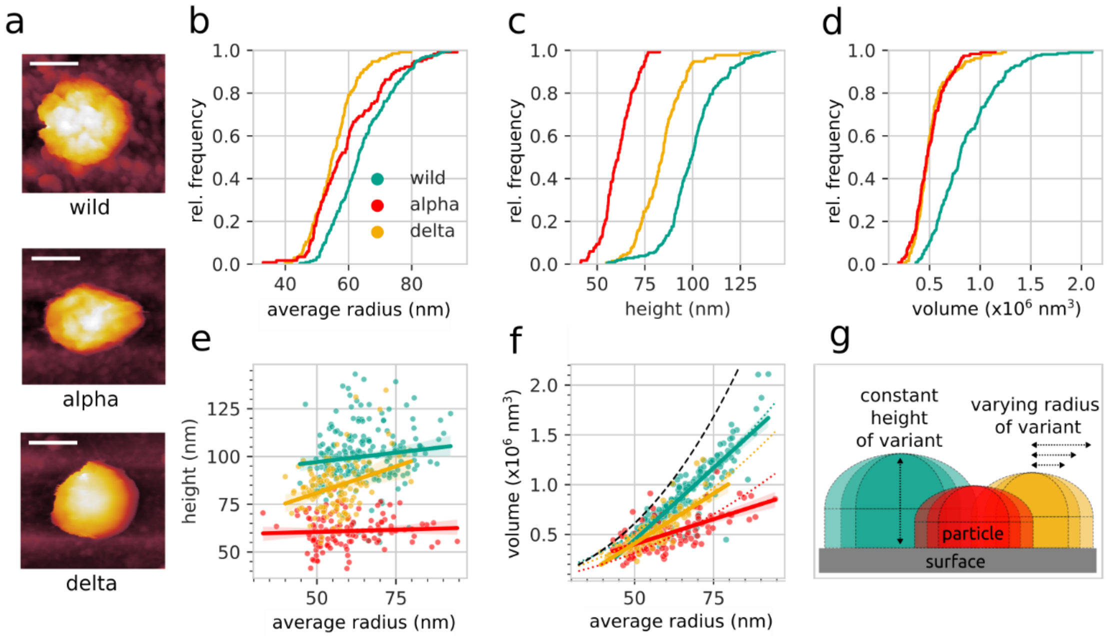

Figure 23. *AFM measurements.* ***a)*** *Representative AFM scans of variants. (scale bar 50 nm). Empirical cumulative distribution functions of* ***b)*** *radius,* ***c)*** *height and* ***d)*** *volume.* ***e)*** *Height vs. radius and* ***f)*** *the volume vs. radius correlations for the different variants (solid lines). Colored dotted curves present the expected volume as a function of radius for 3D shapes presented in* ***g)****. The black dotted curve shows the expected volume for perfect sphere as a function of radius.* ***g)*** *Schematics of the approximate shape of variants expected for perfect non-convoluted AFM. (Adapted from (56))*

Table 2. *Linear correlations between measured topographical parameters. (56)*

variant	**radius vs height**	**radius vs volume**
wild type	0.12	0.89
alpha	0.09	0.71
delta	0.31	0.82

4.2.2. Comparison of variant geometries

To determine the surface-attached equilibrium geometry of the virions, we applied the vesicle model with an added shell representing the corona layer (56) (**Figure 4.** in Introduction and **Figures 15.** and **16.** in Methods)

Visual comparison of the geometrical parameters of fitted variant models is shown in **Figure 24a,b,c**. **Figure 24b** shows the volumes calculated for each variant (56). It can be instantly seen, that the volumes of the *alpha* and *delta* variants are very close to each other, while the volume of the *wild type* is well separated from them. The first four blocks in **Figure 24c** measure the absolute quantities of the given parameters: the primary and secondary contact surfaces (*pc* and *sc*) represent the limiting surface area on the envelope with which the virion can interact with the host through the spike proteins. The receptor contact surface (*rc*) represents the same concept, but from the perspective of the host (so it can be useful for receptor contact calculations if we know the receptor density on the host cell surface). *sc* and *rc* are bounded by the points where the virion's S proteins can still reach the host (see **Figure 15**). Since there is a potential overlap between the corona layer and host surface proteins, and this is a 3D region, it is reasonable to represent it as the contact volume (*cv*) for variant comparison (**Figure 15**).

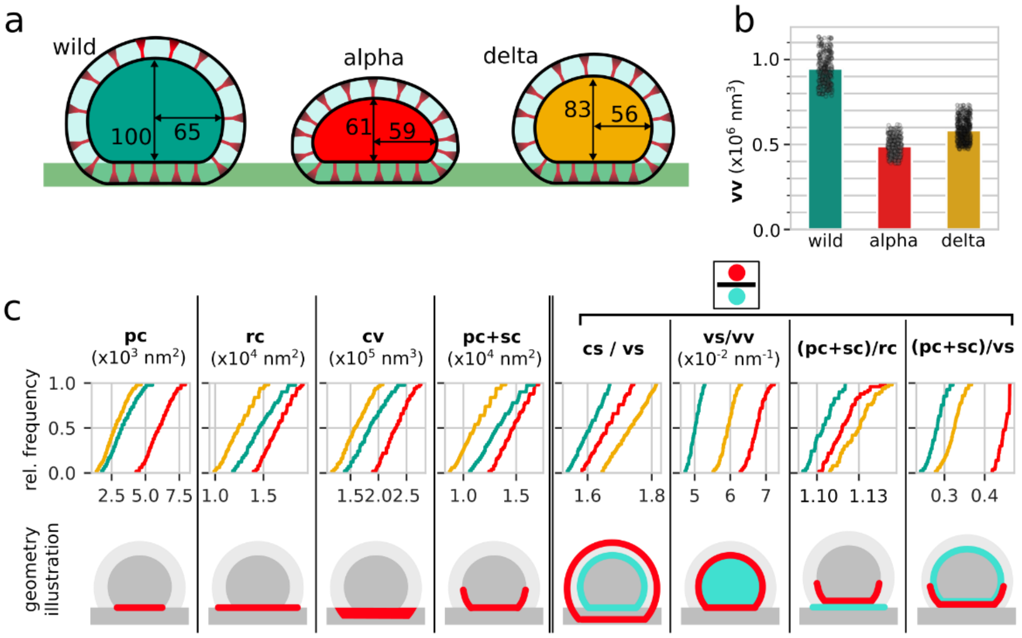

***Figure 24.** Found variant geometries. **a)** The reconstructed shape for each variant according to the vesicle model (the numbers are in nm). **b)** Illustrative topographical samples for each variant. **c)** Upper row shows the empirical distribution of the geometrical parameters derived from the modeled shapes. Lower row illustrates the geometrical meaning of each parameter. (Adapted from (56))*

Besides the absolute quantities, it is more informative to introduce ratios between specific geometrical traits and compare the variants along these quantities (56). These normalized values can better capture the differences on a similar scale. The last four block of **Figure 24c** compares the variants according to defined ratios. The corona surface per vesicle surface ratio (*cs/vs*) quantifies how effectively the S proteins extend the vesicle surface (*vs*), creating a larger surface for potential contacts. The vesicle surface per volume ratio (*vs/vv*) represents how large the interacting surface is compared to the viral cargo, representing an overall measure of how well the virus utilizes available resources for infection. This is also called the specific surface area, which is an important quantity in the study of inorganic materials and nanoparticles (128). Primary + secondary contact surfaces per receptor contact surface ratio (*(pc+sc)/rc*) expresses the ability of the virus to achieve higher spike density on the host surface Finally, primary + secondary contact surfaces per vesicle contact surface ratio *(pc+sc)/vs* reveals what proportion of its total surface a variant can utilize for infection when adhering to a host.

4.2.3. Bending rigidity estimation

The bending rigidity estimation was done as described in the Methods section, see **Figure 16**. The results of bending rigidity estimations can be seen in **Table 3**.

Table 3. *Estimated bending rigidities (κ) for each variant. (56)*

variant	**estimated κ mean ± SD** (10^{-19} J)	**estimated κ median** (10^{-19} J)
alpha	0.8 ± 0.3	0.72
delta	3.6 ± 1.8	3.26
wild type	4.4 ± 2.0	4.04

5. Discussion

5.1. Thick filament topology

At very high levels of KCl concentrations (600 mM), probably due to strong ionic screening, the topographical images reflected the canonical form of muscle *myosin II* with its double headed appearance (56). In this scenario, no thick filaments could be seen in our samples. Decreasing the KCl concentration led to thick filament formation, leading to the classical bipolar *in vivo* sarcomeric thick filament structure.

At low ionic strength, thick filaments often showed a dense core, likely due to additional interactions between neighboring *myosin* motor domains. Filament length increased with KCl concentration and stabilized around 1.5 µm above 100 mM KCl, like *in situ* sarcomeric thick filaments. However, length variation remained high (150 nm to 3.5 µm at 120 mM KCl), indicating the absence of the precise length control seen in the structured environment of muscle.

Apparent filament width also varied with ionic strength and showed significant variability across samples. At 0 mM KCl, filaments were more compact, with about half the width observed at higher salt concentrations. The measured widths exceeded the actual 15 nm shaft diameter due to inclusion of the *myosin* heads in AFM measurements and filament flattening during sample preparation on mica.

5.2. M-complex

5.2.1. Structure

As it was introduced, the *M-complex* functions as an interaction hub formed by *titin* head-to-head oligomers. Our AFM images are in line with the expected hub-like structure of the M complex as can be seen in **Figure 18b**. The topology indicated a structural organization consistent with *myosin*-based spacing, despite the complete absence of *myosin*, likely due to purification. The correlation of *titin* count and *M-complex* volume suggested that *titin* is required for complex formation at a 1:1 stoichiometry (**Figure 18c**). Overall, the *M-complex* is a stable, *titin*-based structural unit reflecting the M-band’s transverse organization around the *myosin* thick filament.

This *M-complex* array likely forms when adjacent *M-complex*es from the M-band lattice remain connected during mechanical disruption of the M-band during *titin* isolation (**Figure 19e,f,g**). The measured inter-complex spacing (~30 nm) is shorter than the typical thick-filament spacing in muscle under physiological conditions (~40 nm) (129-131). Two factors may contribute to this reduced spacing. First, the high ionic strength of the chromatography buffer (~0.6 M) likely screens surface charges, leading to lattice compaction (131). Second, the elastic properties of myomesin—which links *M-complex*es (23, 125, 132, 133)—may allow neighboring complexes to draw closer in a relaxed state, especially, since there are no myosin molecules present.

We deduce that our analyzed *M-complex*es has a broken structure (**Figure 19e,f,g**), this might coincide with the positional instability that has been reported in activated skeletal muscle sarcomeres (134). However, this interpretation remains somewhat speculative, as the precise myomesin content in each *M-complex* is unknown and the isolation process itself might be responsible for the shear and tear stresses that shatter the M-band array. The *titin* filament spacing at the root of the *M-complex* supports the view that the *M-complex* represents the location of the *myosin* thick filament within the M-band (**Figure 19g**), rather than another periodic structure such as M-filaments (124). The measured topographical data allow us to find some resemblance (**Figure 19g**) with the crystallographic structure of the M-band. While this information is highly indirect, it shows the possibility of how the original lattice structure could conserve its structure during isolation.

5.2.2. Nanosurgery of titin filaments

After manipulating *titin* filaments perpendicularly, the stretched molecular strands remained visible on both sides of the tip path, indicating that the displaced segment stabilized on the substrate during or shortly after manipulation. The analysis of heights and lengths of the *nanosurgery* suggested that structural changes such as partial domain unfolding might be taking place during the cutting process.

The results of *nanosurgery* show differences depending on the movement speed of the tip, and this likely reflects how pulling speed affects *titin*'s behavior on the substrate. The outcome of manipulation is governed by the interplay between AFM tip velocity and the molecule’s elasticity, domain unfolding kinetics, and adhesion to the substrate. As *titin* consists of serially linked β-barrel domains (Ig- or FN-type) and unique regions such as the PEVK domain (135), the expected mechanical response includes domain straightening, unfolding, and eventual chain rupture (136). Notably, the nanosurgically manipulated *titin* strands exhibit a non-linear shape, which can be modeled using a slightly modified equation derived from the Kelvin solution described in the Introduction.

5.2.3. Nanosurgery of M-complex

When manipulating the bulk *M-complex*es, we observed that slower cut speed creates a more emphasized material displacement. This provides two important conclusions; if we want to displace as much material as we want, we need very slow tip motion to distribute force propagation as much as possible along the contour of the molecules. On the other hand, if we wish to conduct precisely positioned "surgical cuts", the faster the tip motion, the better and acute the result will be. This is most probably accounted for the highly non-linear force distribution along the molecule, the same phenomenon that was observed when manipulating singular *titin* filaments.

We were able to pull out filaments from the *M-complex* bulk. We found that the end of these filaments can be described with a simple sigmoid as a function of length. The steepness of this transition is described by the coefficient S in the sigmoid, implying increasing structural inhomogeneity and anisotropy as filaments are pulled out. Overall, the *M-complex* acts as a compact, filament-rich supramolecular reservoir that can release extensible strands upon manipulation.

The volume expansion caused by nanomanipulation suggests that nanosurgical manipulation released elastic energy, indicating that the *M-complex* is initially in a compressed state. The compression likely results from adsorption-induced deformation when *titin* oligomers, originally 3-dimensional structures, are flattened, and kinetically trapped onto the mica surface. This supports the idea that myomesin, a key M-band protein, acts as a spacer (21, 23, 26).

The overall behavior suggests dissociation of originally interconnected filaments (**Figure 22a.iii**). While the exact molecular rearrangements remain unclear, the unusual elastic properties of myomesin (132, 137) may contribute. Overall, the *M-complex* exhibits both elastic and plastic mechanical responses, supporting its proposed role in force-bearing functions of the M-band within the sarcomere (21).

5.2.4. Summary of nanosurgery

Our findings are in line with classical molecular mechanics models. To demonstrate this, take the assumed rupture event of filaments as shown in **Figure 25e**. As we proved by measurements, the dislocation is gradual, and the molecule shows a thinning topography, reinforcing the idea of inhomogeneous unfolding. Furthermore, we proved by measurements, that we can approximate the displacement behavior of such filaments using the in-plane force loading model (**Figure 25d**). Moreover, in the Introduction, we described how the alignment of the pulling force direction with the molecule bond direction, and the speed of displacement increases the probability of rupture (Bell model). If we inspect **Figure 25d**, we can see that as we take a position on the displaced filament, the closer we go to the pulling probe, the more aligned the angle becomes with the pulling force. Moreover, the displacement is nonlinearly increasing closer to the pulling probe, and if the displacement takes the same time for every part of the filament, the pulling velocity is greater closer to the probe, and higher speed leads to higher forces. These two observations (angle and speed) explain our intuition on why the filaments rupture or unfold closer to the pulling probe. The displacement model is capable of estimating the Poisson's ratio or Young's modulus (the constant in **Eq.3**), but I did not use it for such a purpose in my work.

We observed that the outreaching *titin* molecules were shorter than singular *titin* molecules. This could be explained with the constrained nature of *titin* within the *M-complex*. The constraints are the specific architecture and the excluded volume effects in the bulk. Theoretically, this is in line with the WLC model experiments that show that within a crowded environment, the proteins are not intrinsically equilibrated. They are still in equilibrium, but this equilibrium is forced by the complex and intermolecular interactions (see **Figure 8b**).

According to our measurements, the bulk molecular complex behaves as a ductile material, showing necking as described in **Figure 22c.iii**. As we finished the *nanosurgery*, the molecule falls into a fixed position, and it is ambiguous whether this fixation is due to a kinetic trapping, or a true plastic change. One possible way to uncover the truth is to change the ionic environment around the cut and do a follow-up imaging whether the filament crawls back to an unextended equilibrium form.

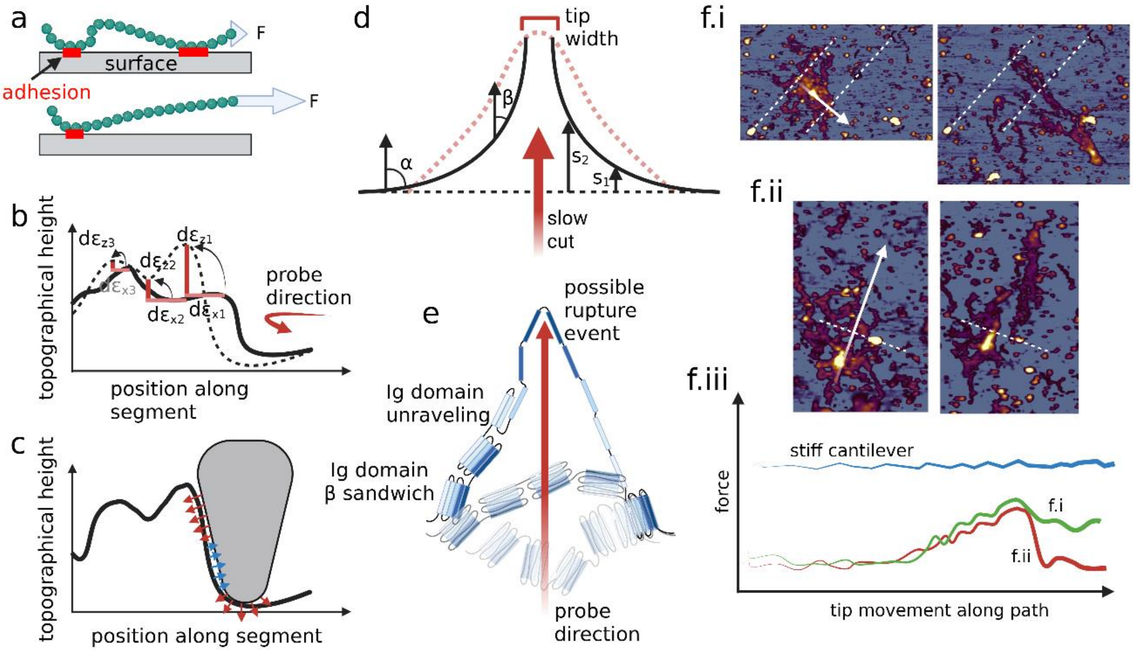

Figure 25. *Nanosurgery observations and future directions.* ***a)*** *Adhesion characteristics of molecules during nanosurgery. The pulling force distribution and mechanical response is dependent on adhesion.* ***b)*** *Topographical changes during nanosurgery. The solid line is the original topography, and the dashed line is the manipulated topography. The different manipulated parts seem to have a different effective Poisson's ratio.* ***c)*** *Finer heterogeneous interaction between the molecules and the tip.* ***d)*** *The filament displacement calculated from the Kelvin solution (black). The angles and distances help us to deduce where the breaking probability is the highest. The red dashed curve is a theoretic example, where the molecule is only weakly adhered and an FJC displacement might better describe the mechanics.* ***e)*** *Illustration of the different molecular configurations during nanosurgery.* ***f.i)*** *Nanosurgery in liquid phase, where the whole M-complex way displaced during manipulation and it remained intact. The dashed white lines help to grasp the extent of the displacement.* ***f.ii)*** *A scenario, where the tip ripped out a part of the M-complex and took it to a distance. The original M-complex extended in the middle as can be seen.* ***f.iii)*** *The expected force measurements during different nanosurgery scenarios. For a stiff cantilever, forces on the pN scale cannot produce meaningful signals. For the* ***f.i)*** *scenario, we would expect the force curve to first rise and then stay around the same value as we drag the whole complex along the way. For the* ***f.ii)*** *scenario, we would expect the force curve to rise, then fall down after the rip-out event, but not to 0, since we are still carrying part of the M-complex. (Created with Biorender.com)*

Further interesting qualitative material behavior can be deduced from our measurements presented in **Figure 25b**. After a specific L shaped nanosurgical cut in the molecule, the topographical appearance (at the kink of the L shape) changes in a way, from which we can deduce the Poisson's ratio of the complex. This apparent Poisson's ratio is nonlinearly changing as we can see on **Figure 25b**.

There are several limitations of our methodology. First, most AFM vendors do not provide streamlined and precise measurement protocols and software solutions for lateral force measurements, this makes it cumbersome to convert cantilever lateral deflection into valid force data. The other limitation is, even if the deflection-force conversion is done, most cantilever for dry measurement are too stiff to detect the lateral torsion caused by pN scale forces of protein pulling (**Figure 25f.iii**). This limitation can be overcome by conducting liquid measurements with the proper ionic conditions (**Figure 25f**). This changes the apparent nanomechanics and makes the underlying forces detectable with less stiff probes.

A more precise description is needed about how the *nanosurgery* procedure affects the molecule, as it should be able to explain how large the adhesion forces are between the molecule and the surface (**Figure 25a**). For this, one could set up two boundary states, one where the molecule is strongly adhered, almost as it would be part of the surface. Manipulated filament shapes for this state could be well approximated with the Kelvin solution as demonstrated. When the molecule adherence is very small, then the manipulated filament shape could be approximated as an extensible WLC or FJC. Using these boundary states, we could assign a measure of how strong the adhesion is. The possible difference of such curves is depicted in **Figure 25d**, and manipulations with low adhesion in liquid is shown in **Figure 25f.i, f.ii**.

Another limitation arises as during tip-sample contact, the exact geometrical configuration is unknown, thus it is hard to tell that what forces act locally along the surface of the tip (**Figure 25c**). Solving this problem and the collection of such interaction data could bring in a new level of complexity to explain what the is the exact pull and push dynamics along the contact surface are.

An essential next step in our research is the integration of molecular dynamics (MD) simulations. These can support experimental design and offer bottom-up explanations for our observations. Given the size of the molecular systems involved—often large complexes or synthetic constructs—a hybrid approach combining coarse-grained modeling with atomic- or quantum-level simulations at key interaction sites could yield valuable insights into tip-sample mechanics.

Why is *nanosurgery* the future? As biomedical research shifts from statistical models to single-molecule resolution, there's a growing demand for precise molecular positioning. With shrinking sensor scales, techniques like *nanosurgery*—using an AFM tip to mechanically position molecules with nanometer accuracy—will become increasingly relevant. For instance, in our *M-complex*–thick filament experiments, this level of control could be the foundation for probing protein interactions at unprecedented detail, alongside tools like optical tweezers.

5.3. Thick-filament and M-complex interaction

Using AFM, we found no evidence of regular alignment or direct binding of *myosin* along *titin* molecules under a range of ionic strengths or after mechanical straightening. Instead, *titin* and *myosin* primarily formed separate populations, indicating that their self-association is favored over cross-binding. These findings differ from earlier reports suggesting interaction at the *myosin* tail’s C-terminus (138). The discrepancy may stem from the mechanical forces (144–400 pN) applied during meniscus stretching, which could disrupt weak or transient interactions.

Under conditions allowing configurational relaxation, *titin* oligomers appeared to bind the surface of preformed thick filaments, forming a mesh-like layer. Our observations suggest that *titin* does not serve as a geometric template but may regulate thick filament length indirectly, by forming a structural wrapping (scaffold) that restricts filament growth and stabilizes filament ends. This model provides an alternative mechanism to explain *titin*’s role in sarcomeric architecture, extending recent structural findings in cardiac muscle (31).

5.4. Coronavirus variants

The range of the measured quantities are comparable with published geometrical parameters of coronaviruses, but the variants have noticable differences in their geometries. Correlation analysis between height and radius suggests that the variability of height of a given variant is not explained by the variability of the radius in this range. This observation suggests that height reflects a more fundamental (invariant) property, such as the nanomechanical behavior of the given variant. The volume vs. radius correlation shows that as the radius increases for each variant, the volume increase is constrained differently, again indicating a different nanomechanical behavior per variant. The measured circularities of the variants show no difference, indicating that the equilibrium shape is circular (oblate in 3D) with only slight perturbations, which may be attributed to the pleomorphic behavior. We assume that, from sample preparation to measurement, the virions reached an equilibrium shape.

The vesicle model, together with the corona layer provided interesting insights into the geometrical traits for each variants. Variants are definitely smaller in size compared to the *wild type* coronavirus. Our defined geometrical parameters and ratios emphasize the structural optimization of the virus focusing on the virus-host interaction. Overall, the *alpha* and *delta* variants seem to dominate our defined geometrical traits (e.g., specific surface area or contact surface relative to the virion surface) over the *wild type*, suggesting that these shape parameters are important in optimizing and enhancing infectivity. According to our measurements, the *alpha* variant has the most deflated envelope. It must be emphasized that these small absolute and relative geometrical differences are amplified by the huge and exponential viral load, that is, the millions of virions produced in the host organisms, making these small differences matter significantly on a large scale.

Our bending rigidity estimation results are close to previous estimations of coronavirus and influenza virions determined by simulations (57, 108). This underlines the credibility and validity of the introduced method. Furthermore, these estimates provide a quantitative basis for the nanomechanical differences between the variants. The relatively large SD of the estimates is due to the high (± 9 nm) tolerance for the model fitting.

According to our results, the bending rigidities suggest that the nanomechanical differences between the *delta* vs. *wild type* is of order 10^{-20} J, while the differences between *alpha* vs. (*delta* and *wild*) is an order of magnitude higher, 10^{-19} J. We recall that the difference of measured volumes for *alpha* vs. *delta* variants is of the order 10^4 nm^3, and the *wild* vs (*alpha* and *delta*) difference is an order of magnitude higher, 10^5 nm^3. Thus, the bending rigidity and volume tendencies are different among the variants (**Figure 26c**), indicating that these virion traits might be the result of different biological processes. The *delta* variant is nanomechanically closer to the *wild type* than *alpha*, but in the volume dimension, *alpha* and *delta* are closer to each other than to the *wild type*. Literature indicates virion stiffness and membrane nanomechanics to be quite important throughout the infection due to different physicochemical phenomena (139, 140). Some antiviral chemical causes stiffening of the virion membrane (48). The virus having a less rigid membrane might be a significant advantage in infection (139).

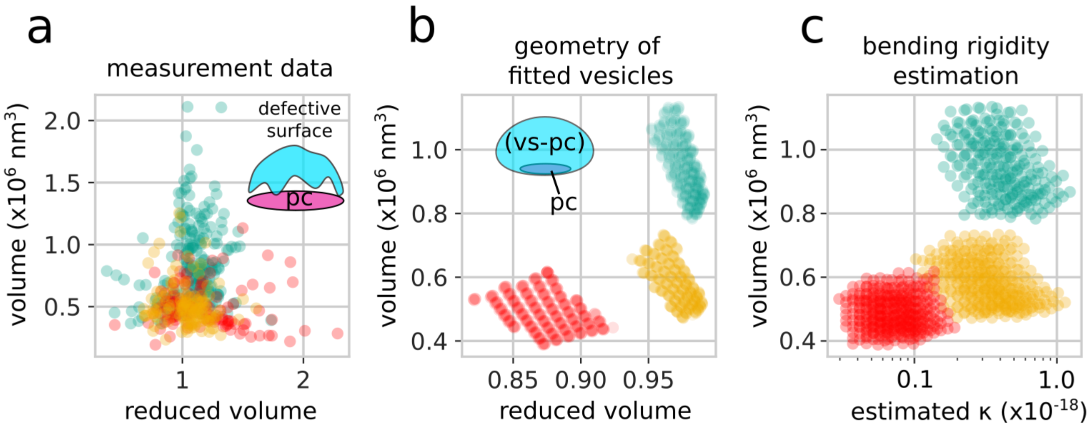

Figure 26. *Overview of the study and numerical results. Reduced volume is a dimensionless quantity expressing how closely a 3D object resembles a perfect sphere. The smaller the, the more deflated the vesicle is. Its maximal value is 1.* ***a)*** *Illustration of how unreliable the original reduced volume values are, since the measured surface and projected areas are too noisy and can even miss surfaces (due to mask cutoff) on the sides of the virions (inset).* ***b)*** *After fitting the model on means per variant, the geometrical data becomes meaningful; furthermore, it can be used to estimate the bending rigidities* ***c)****. Estimation results for each variants (color coding is* ***teal****=wild,* ***red****=alpha,* ***orange****=delta). (Adapted from (56))*

Topographical AFM imaging has limitations, including its projective nature—capturing only surface heights—and convolution effects from tip shape. However, incorporating prior knowledge about the scanned objects, such as virions, can improve interpretation. To obtain more realistic shapes, we applied an equilibrium vesicle shape model (**Figure 4**). As shown in **Figure 26a–c**, this approach enhances result clarity: raw reduced volume values were invalid (>1) and indistinguishable (**Figure 26a**), but model fitting and averaging produced valid and distinct values (**Figure 26b**). Moreover, our method enables estimation of bending rigidities for each variant (**Figure 26c**).

6. Conclusion

The thesis explored a wide spectrum of AFM biological experiments on the mesoscale, from single molecules to more complex multimolecular structures, exploring the self-, intermolecular- and surface interactions of these molecular species. One part of the thesis concentrated on striated muscle specific *myosin II* molecules and *titins*, as well as on the larger, sarcomere derived *M-complex*. The other part of the thesis focused on the structure of SARS-CoV-2, an enveloped virus responsible for the recent pandemic. The common characteristic of the observed multimolecular specimens is how the different components produce a generative effect when they assemble into complexes. Symmetry, stability and function emerges from individual, non-symmetric elements. Moreover, this emergent structure is incorporated in a dynamic biological and physical landscape of immense scale. As opposed to a pure reductionist approach, my research tried to grasp these molecular systems as a whole. The work reflects the advantages and disadvantages of such an approach (e.g. observing continuum mechanical phenomena emerging from a molecular complex). Our approach proved that the system-scale experimentation allows to uncover physical properties that remain hidden when only the components are observed.

We showed that the *M-complex* is a stable, *titin*-based structural hub, consistent with M-band organization. Despite the absence of *myosin*, the measured spacing and lattice patterns resemble physiological M-band arrangements. Our *nanosurgery* approach enabled controlled mechanical manipulation, revealing domain-level behavior and filament dynamics. Manipulated *titin* filaments exhibited structural deformation consistent with unfolding and showed velocity-dependent mechanical responses. The shape and displacement of these filaments were accurately described using a continuum mechanical model.

AFM *nanosurgery* of the *M-complex* demonstrated both plastic and elastic responses and revealed a compact filament reservoir capable of releasing extensible strands. The *M-complex* appears to store elastic energy, likely due to surface-induced deformation and kinetic trapping. Observed necking and post-manipulation fixation suggest ductile-like behavior at the mesoscale. Shortened *titin* extensions and spatial constraints indicate restricted equilibrium in the complex interior. Theoretical comparisons with Bell model and in-plane force loading help explain rupture patterns near the pulling tip.

We observed how the environmental conditions (buffer concentration) oblige single *myosin II* molecules to form rudimentary thick filaments. These thick filaments resembled the *in vivo* forms, but without spatial restrictions which led to *myosin* assemblies different from the assumed sarcomeric layout. We concluded that, for proper thick filament formation, more components are required. Based on the *in vivo* topological proximity and interconnection of *titin* and *M-complex* with the thick filaments, we explored how *M-complex* interacts with the *myosin II* molecules.

Notably, *titin* and *myosin* did not co-assemble under standard conditions, but *titin* oligomers bound thick filaments after relaxation. These findings suggest *titin*'s role is more regulatory than templating, contributing to filament length control through structural confinement.

Methodological limitations, particularly in lateral force calibration and tip-sample geometry, highlight the need for more refined tools. Addressing these challenges could improve force quantification and dynamic modeling. Future work should integrate molecular dynamics simulations to resolve local interactions and structural transitions. Coarse-grained and atomic models could provide bottom-up insight into nanosurgical manipulation.

Nanosurgery offers a powerful platform for probing protein mechanics and spatial interactions at single-molecule resolution. As molecular-level precision becomes increasingly relevant in nanotechnology and biomedical research, techniques like this will be vital. Our results underline the *M-complex*'s mechanical complexity and support its role in sarcomeric force transmission and structural maintenance.

Our AFM-based analysis revealed distinct structural and mechanical differences among SARS-CoV-2 variants. The *alpha* variant showed the lowest height and volume, while the *wild type* exhibited the largest values across all measured geometric parameters, with *delta* consistently in between. These differences suggest that virion morphology varies meaningfully between variants, possibly influencing infectivity or environmental stability.

Geometric modeling using a vesicle-plus-corona approach allowed detailed comparisons of surface area usage. Normalized ratios provided insight into how effectively each variant may engage with host cells, with *alpha* and *delta* showing more infection-optimized geometries than the *wild type*.

Finally, by fitting vesicle models to the virion shapes, we estimated bending rigidity (κ), finding the *wild type* to have the highest membrane stiffness, followed by *delta* and *alpha*. These nanomechanical differences may reflect underlying structural or compositional adaptations in each variant, contributing to their distinct biological behaviors.

7. Summary

My research used AFM and nanosurgery to investigate the structural and mechanical properties of the sarcomeric M-complex and associated proteins. The M-complex was confirmed to be a stable, titin-based hub, displaying elastic and plastic responses under mechanical manipulation. Nanosurgery revealed unfolding behaviors in titin filaments, deformation patterns, and rupture dynamics consistent with continuum mechanical models and force-loading theories. While myosin formed physiologically relevant structures, the thick-filament spatial organization deviated from the sarcomeric layout *in vitro.* Interestingly, titin and myosin did not co-assemble under standard conditions, but M-complexes interacted with thick filaments after relaxation, supporting a regulatory rather than scaffolding role for titin in filament organization.

AFM analysis of SARS-CoV-2 variants further demonstrated the technique's utility in virology. Morphological differences between alpha, delta, and wild type virions were clearly resolved, with alpha being the most compact and wild type being the largest. Using a vesicle-plus-corona model, geometrical ratios suggested alpha and delta variants have more efficient host interaction surfaces. Bending rigidity estimates revealed variant-specific membrane stiffness, with the wild type being most rigid. These structural and mechanical distinctions may reflect functional adaptations influencing viral infectivity and stability.

8. References

1. Pan N. Exploring the significance of structural hierarchy in material systems-A review. Appl Phys Rev. 2014;1.

2. Korenić A, Perović S, Ćirković MM, Miquel P-A. Symmetry breaking and functional incompleteness in biological systems. Prog Biophys Mol. 2020;150:1-12.

3. Konieczny L, Roterman-Konieczna I, Spólnik P. Systems Biology: Functional Strategies of Living Organisms. Cham (CH): Springer; 2023. p. 1-52.

4. Li Y, Tian R, Zou Y, Wang T, Liu J. Strategies and Applications for Supramolecular Protein Self-Assembly. Chem Eur J. 2024;30(66):e202402624.

5. Hopkin K, Johnson AD, Morgan D, Raff M, Roberts K, Walter P. Essential Cell Biology: Fifth International Student Edition. New York: W.W. Norton; 2018. p. 83-171.

6. Kessel A, Ben-Tal N. Introduction to Proteins: Structure, Function, and Motion, Second Edition. Boca Raton, Florida: CRC Press; 2018. p. 64-194.

7. Granzier HL, Labeit S. Discovery of Titin and Its Role in Heart Function and Disease. Circ Res. 2025;136(1):135-57.

8. Das N, Khan T, Halder B, Ghosh S, Sen P. Macromolecular crowding effects on protein dynamics. Int J Biol Macromol. 2024;281:136248.

9. Song J. In the Beginning: Let Hydration Be Coded in Proteins for Manifestation and Modulation by Salts and Adenosine Triphosphate. Int J Mol Sci. 2024;25(23).

10. Laage D, Elsaesser T, Hynes JT. Water Dynamics in the Hydration Shells of Biomolecules. Chem Rev. 2017;117(16):10694-725.

11. Panja AS, Maiti S, Bandyopadhyay B. Protein stability governed by its structural plasticity is inferred by physicochemical factors and salt bridges. Sci Rep. 2020;10(1):1822.

12. Balcão VM, Vila MMDC. Structural and functional stabilization of protein entities: state-of-the-art. Adv Drug Deliver Rev. 2015;93:25-41.

13. He X, Ewing AG. Hofmeister Series: From Aqueous Solution of Biomolecules to Single Cells and Nanovesicles. ChemBioChem. 2023;24(9):e202200694.

14. Rabe M, Verdes D, Seeger S. Understanding protein adsorption phenomena at solid surfaces. Adv Colloid Interfac. 2011;162(1):87-106.

15. Rajan R, Ahmed S, Sharma N, Kumar N, Debas A, Matsumura K. Review of the current state of protein aggregation inhibition from a materials chemistry perspective: special focus on polymeric materials. Mater Adv. 2021;2:1139-76.

16. Kachur TM, Pilgrim DB. Myosin assembly, maintenance and degradation in muscle: Role of the chaperone UNC-45 in myosin thick filament dynamics. Int J Mol Sci. 2008;9(9):1863-75.

17. Ojima K. Myosin: Formation and maintenance of thick filaments. Anim Sci J. 2019;90(7):801-7.

18. Ahmed RE, Tokuyama T, Anzai T, Chanthra N, Uosaki H. Sarcomere maturation: function acquisition, molecular mechanism, and interplay with other organelles. Philos Trans R Soc B, Biol Sci. 2022;377(1864):20210325.

19. Tamborrini D, Wang Z, Wagner T, Tacke S, Stabrin M, Grange M, et al. Structure of the native myosin filament in the relaxed cardiac sarcomere. Nat. 2023;623(7988):863-71.

20. Mukund K, Subramaniam S. Skeletal muscle: A review of molecular structure and function, in health and disease. WIREs Syst Biol Med. 2020;12(1):e1462.

21. Lange S, Pinotsis N, Agarkova I, Ehler E. The M-band: The underestimated part of the sarcomere. Biochim Biophys Acta Mol Cell Res. 2020;1867(3):118440.

22. Lamber EP, Guicheney P, Pinotsis N. The role of the M-band myomesin proteins in muscle integrity and cardiac disease. J Biomed Sci. 2022;29(1):18.

23. Agarkova I, Perriard J-C. The M-band: an elastic web that crosslinks thick filaments in the center of the sarcomere. Trends Cell Biol. 2005;15(9):477-85.

24. Pernigo S, Fukuzawa A, Bertz M, Holt M, Rief M, Steiner RA, et al. Structural insight into M-band assembly and mechanics from the titin-obscurin-like-1 complex. PNAS. 2010;107(7):2908-13.

25. Pernigo S, Fukuzawa A, Beedle A, Holt M, Round A, Pandini A, et al. Binding of Myomesin to Obscurin-Like-1 to the Muscle M-Band Provides a Strategy for Isoform-Specific Mechanical Protection. Structure. 2016;25.

26. Agarkova I, Ehler E, Lange S, Schoenauer R, Perriard JC. M-band: a safeguard for sarcomere stability? J Muscle Res Cell Motil. 2003;24(2-3):191-203.

27. Shabarchin AA, Tsaturyan AK. Proposed role of the M-band in sarcomere mechanics and mechano-sensing: a model study. BMMB. 2010;9(2):163-75.

28. Lange S, Xiang F, Yakovenko A, Vihola A, Hackman P, Rostkova E, et al. The Kinase Domain of Titin Controls Muscle Gene Expression and Protein Turnover. Science (New York, NY). 2005;308:1599-603.

29. McNamara JW, Parker BL, Voges HK, Mehdiabadi NR, Bolk F, Ahmad F, et al. Alpha kinase 3 signaling at the M-band maintains sarcomere integrity and proteostasis in striated muscle. Nat Cardiovasc Res. 2023;2(2):159-73.

30. Lange S, Agarkova I, Perriard J-C, Ehler E. The sarcomeric M-band during development and in disease. J Muscle Res Cell Motil. 2005;26:375-9.

31. Tonino P, Kiss B, Strom J, Methawasin M, Smith JE, 3rd, Kolb J, et al. The giant protein titin regulates the length of the striated muscle thick filament. Nat Commun. 2017;8(1):1041.

32. Squarci C, Bianco P, Reconditi M, Pertici I, Caremani M, Narayanan T, et al. Titin activates myosin filaments in skeletal muscle by switching from an extensible spring to a mechanical rectifier. PNAS. 2023;120(9):e2219346120.

33. Linke WA. Stretching the story of titin and muscle function. J Biomech. 2023;152:111553.

34. Rabaan AA, Alenazy MF, Alshehri AA, Alshahrani MA, Al-Subaie MF, Alrasheed HA, et al. An updated review on pathogenic coronaviruses (CoVs) amid the emergence of SARS-CoV-2 variants: A look into the repercussions and possible solutions. J Infect Public Health. 2023;16(11):1870-83.

35. Mingaleeva RN, Nigmatulina NA, Sharafetdinova LM, Romozanova AM, Gabdoulkhakova AG, Filina YV, et al. Biology of the SARS-CoV-2 Coronavirus. Biochem (Mosc). 2022;87(12):1662-78.

36. El-Kassas M, Alboraie M, Elbadry M, El Sheemy R, Abdellah M, Afify S, et al. Non-pulmonary involvement in COVID-19: A systemic disease rather than a pure respiratory infection. World J Clin Cases. 2023;11(3):493-505.

37. Bak A, Mugglestone MA, Ratnaraja NV, Wilson JA, Rivett L, Stoneham SM, et al. SARS-CoV-2 routes of transmission and recommendations for preventing acquisition: joint British Infection Association (BIA), Healthcare Infection Society (HIS), Infection Prevention Society (IPS) and Royal College of Pathologists (RCPath) guidance. J Hosp Infect. 2021;114:79-103.

38. Ziebuhr J. Coronaviruses. Advances in Virus Research. London: Elsevier Science & Technology; 2016. p. 1-40.

39. Hardenbrook NJ, Zhang P. A structural view of the SARS-CoV-2 virus and its assembly. Curr Opin Virol. 2022;52:123-34.

40. Erkihun M, Ayele B, Asmare Z, Endalamaw K. Current Updates on Variants of SARS-CoV- 2: Systematic Review. Health Sci Rep. 2024;7(11):e70166.

41. Markov PV, Ghafari M, Beer M, Lythgoe K, Simmonds P, Stilianakis NI, et al. The evolution of SARS-CoV-2. Nat Rev Microbiol. 2023;21(6):361-79.

42. Meyerowitz EA, Richterman A. SARS-CoV-2 Transmission and Prevention in the Era of the Delta Variant. Infect Dis Clin North Am. 2022;36(2):267-93.

43. World Health O. Updated working definitions and primary actions for SARS-CoV-2 variants. World Health Organization; 2023.

44. Perez-Gomez R. The Development of SARS-CoV-2 Variants: The Gene Makes the Disease. J Dev Biol. 2021;9(4).

45. Narayanan SA, Jamison DA, Guarnieri JW, Zaksas V, Topper M, Koutnik AP, et al. A comprehensive SARS-CoV-2 and COVID-19 review, Part 2: host extracellular to systemic effects of SARS-CoV-2 infection. Eur J Hum Genet. 2024;32(1):10-20.

46. Obermeyer F, Jankowiak M, Barkas N, Schaffner SF, Pyle JD, Yurkovetskiy L, et al. Analysis of 6.4 million SARS-CoV-2 genomes identifies mutations associated with fitness. Sci. 2022;376(6599):1327-32.

47. Zhang Z, Nomura N, Muramoto Y, Ekimoto T, Uemura T, Liu K, et al. Structure of SARS-CoV-2 membrane protein essential for virus assembly. Nature Communications. 2022;13(1):4399.

48. Mateu MG. Structure and Physics of Viruses: An Integrated Textbook. Dordrecht, Netherlands: Springer Netherlands; 2013. p. 519-51.

49. Phillips R, Kondev J, Theriot J, Garcia H. Physical Biology of the Cell. New York: CRC Press; 2012. p. 427-75.

50. Dimova R, Marques C. The Giant Vesicle Book. Boca Raton, Florida: CRC Press; 2019. p. 55-146.

51. Capovilla R, Guven J, Santiago JA. Deformations of the geometry of lipid vesicles. J Phys. 2003;36(23):6281.

52. Seifert U, Lipowsky R. Adhesion of vesicles. Phys Rev A. 1990;42(8):4768-71.

53. Seifert U, Berndl K, Lipowsky R. Shape transformations of vesicles: Phase diagram for spontaneous- curvature and bilayer-coupling models. Phys Rev A. 1991;44(2):1182-202.

54. Tordeux C, Fournier JB, Galatola P. Analytical characterization of adhering vesicles. Phys Rev E. 2002;65(4):041912.

55. Helfrich W. Elastic properties of lipid bilayers: theory and possible experiments. Z Naturforsch C. 1973;28(11):693-703.

56. Sziklai D, Budavári B, Kiss B, Herényi L, Kiss Z, Pályi B, et al. Unveiling the Structural and Mechanical Diversity of SARS-CoV-2 Variants Using Atomic Force Microscopy. In Preparation. 2025.

57. García-Arribas AB, Ibáñez-Freire P, Carlero D, Palacios-Alonso P, Cantero-Reviejo M, Ares P, et al. Broad Adaptability of Coronavirus Adhesion Revealed from the Complementary Surface Affinity of Membrane and Spikes. Adv Sci. 2024;11(41):2404186.

58. Kiss B, Kis Z, Pályi B, Kellermayer MSZ. Topography, Spike Dynamics, and Nanomechanics of Individual Native SARS-CoV-2 Virions. Nano Lett. 2021;21(6):2675-80.

59. Wang B, Zhong C, Tieleman DP. Supramolecular Organization of SARS-CoV and SARS-CoV-2 Virions Revealed by Coarse-Grained Models of Intact Virus Envelopes. J Chem Inf Model. 2022;62(1):176-86.

60. Hu Y, Buehler MJ. Comparative Analysis of Nanomechanical Features of Coronavirus Spike Proteins and Correlation with Lethality and Infection Rate. Matter. 2021;4(1):265-75.

61. Reifenberger RG. Fundamentals Of Atomic Force Microscopy - Part I: Foundations. Singapore: World Scientific Publishing Company; 2015. p. 1-18.

62. Eaton P, West P. Atomic Force Microscopy. Oxford: Oxford University Press; 2010. p. 9-81.

63. Gołek F, Mazur P, Ryszka Z, Zuber S. AFM image artifacts. Appl Surf Sci. 2014;304:11-9.

64. Christenson HK, Thomson NH. The nature of the air-cleaved mica surface. Surf Sci Rep. 2016;71(2):367-90.

65. Morita S, Wiesendanger R, Meyer E. Noncontact Atomic Force Microscopy. Berlin, Heidelberg: Sringer-Verlag; 2002. p. 11-46.

66. Wang X, Ramírez-Hinestrosa S, Dobnikar J, Frenkel D. The Lennard-Jones potential: when (not) to use it. PCCP. 2020;22(19):10624-33.

67. Ahmine AN, Bdiri M, Féréol S, Fodil R. A comprehensive study of AFM stiffness measurements on inclined surfaces: theoretical, numerical, and experimental evaluation using a Hertz approach. Sci Rep. 2024;14(1):25869.

68. Zhang K, Bai Y, Zhang Z. Compensation Method for Correcting the Topography Convolution of the 3D AFM Profile Image of a Diffraction Grating. Machines. 2024;12(2):126.

69. Villarrubia JS. Scanned probe microscope tip characterization without calibrated tip characterizers. J Vac Sci Technol B. 1996;14(2):1518-21.

70. Villarrubia JS. Algorithms for Scanned Probe Microscope Image Simulation, Surface Reconstruction, and Tip Estimation. J Res Natl Inst Stand Technol. 1997;102(4):425-54.

71. Landau LD, Landau LD, Lifshit︠s︡ EM, Kosevich AM, Lifshitz EM, Pitaevskii LP. Theory of Elasticity: Volume 7. Oxford: Butterworth-Heinemann; 1986. p. 1-26.

72. Mazars M. Statistical physics of the freely jointed chain. Phys Rev E. 1996;53(6):6297-319.

73. Buche MR, Silberstein MN, Grutzik SJ. Freely jointed chain models with extensible links. Phys Rev E. 2022;106(2):024502.

74. Marantan A, Mahadevan L. Mechanics and statistics of the worm-like chain. Am J Phys. 2018;86(2):86-94.

75. Bahar I, Jernigan RL, Dill KA. Protein Actions: Principles and Modeling. New York: Garland Science, Taylor & Francis Group, LLC; 2017. p. 1-100.

76. Jaenicke R. Stability and stabilization of globular proteins in solution. J Biotech. 2000;79(3):193-203.

77. Lubarda MV, Lubarda VA. Intermediate Solid Mechanics. Cambridge: Cambridge University Press; 2020. p. 1-80.

78. Pajic-Lijakovic I, Milivojevic M, McClintock PVE. Compressibility of biological systems: the viscoelastic Poisson’s ratio. Adv Phys. 2025;10(1):2440023.

79. Till M, Ullmann G. McVol – A Program for Calculating Protein Volumes and Identifying Cavities by a Monte Carlo Algorithm. J Mol Model. 2010;16:419-29.

80. Chen C, Makhatadze G. ProteinVolume: Calculating molecular van der Waals and void volumes in proteins. BMC Bioinformatics. 2015;16:1-6.

81. Koehl P, Akopyan A, Edelsbrunner H. Computing the Volume, Surface Area, Mean, and Gaussian Curvatures of Molecules and Their Derivatives. J Chem Inf Model. 2023;63(3):973-85.

82. Wang X, Kou Z, Qiao R, Long Y, Li B, Li X, et al. Many-body van der Waals interactions in multilayer structures studied by atomic force microscopy. Nature Communications. 2025;16(1):324.

83. Herzog W. The multiple roles of titin in muscle contraction and force production. Biophys Rev. 2018;10(4):1187-99.

84. Kellermayer MS, Grama L. Stretching and visualizing titin molecules: combining structure, dynamics and mechanics. J Muscle Res Cell Motil. 2002;23(5-6):499-511.

85. Sun H, Guo Z, Hong H, Yu P, Xue Z, Chen H. Protein folding mechanism revealed by single-molecule force spectroscopy experiments. Biophys Rep. 2021;7(5):399-412.

86. Zuo J, Li H. Two-Molecule Force Spectroscopy on Proteins. ACS Nano. 2023;17(8):7872-80.

87. Hakari T, Sekiguchi H, Osada T, Kishimoto K, Afrin R, Ikai A. Nonlinear displacement of ventral stress fibers under externally applied lateral force by an atomic force microscope. Cytoskeleton (Hoboken). 2011;68(11):628-38.

88. Favata A. On the Kelvin Problem. J Elast. 2012;109:189-204.

89. Kachanov ML, Shafiro B, Tsukrov I. Handbook of Elasticity Solutions. Dordrecht, Netherlands: Springer Netherlands; 2003. p. 53-75.

90. Hughes ML, Dougan L. The physics of pulling polyproteins: a review of single molecule force spectroscopy using the AFM to study protein unfolding. Rep Prog Phys. 2016;79(7):076601.

91. Hoffmann T, Tych KM, Hughes ML, Brockwell DJ, Dougan L. Towards design principles for determining the mechanical stability of proteins. PCCP. 2013;15(38):15767-80.

92. Buehler MJ, Ackbarow T. Fracture mechanics of protein materials. Mater Today. 2007;10(9):46-58.

93. Bell GI. Models for the Specific Adhesion of Cells to Cells. Sci. 1978;200(4342):618-27.

94. Bullerjahn JT, Sturm S, Kroy K. Theory of rapid force spectroscopy. Nature Communications. 2014;5(1):4463.

95. Kellermayer MS, Smith SB, Granzier HL, Bustamante C. Folding-unfolding transitions in single titin molecules characterized with laser tweezers. Sci. 1997;276(5315):1112-6.

96. Soteriou A, Gamage M, Trinick J. A survey of interactions made by the giant protein titin. J Cell Sci. 1993;104 (Pt 1):119-23.

97. Sziklai D, Sallai J, Papp Z, Kellermayer D, Mártonfalvi Z, Pires RH, et al. Nanosurgical Manipulation of Titin and Its M-Complex. Nanomaterials (Basel). 2022;12(2):178.

98. Warren CM, Krzesinski PR, Greaser ML. Vertical agarose gel electrophoresis and electroblotting of high-molecular-weight proteins. J Electrophor. 2003;24(11):1695-702.

99. Kellermayer M, Sziklai D, Papp Z, Decker B, Lakatos E, Mártonfalvi Z. Topology of interaction between titin and myosin thick filaments. J Struct Biol. 2018;203(1):46-53.

100. Mártonfalvi Z, Kellermayer M. Individual Globular Domains and Domain Unfolding Visualized in Overstretched Titin Molecules with Atomic Force Microscopy. PLoS One. 2014;9(1):e85847.

101. Margossian SS, Lowey S. Preparation of myosin and its subfragments from rabbit skeletal muscle. Methods Enzymol. 1982;85 Pt B:55-71.

102. Koretz JF. Methods in Enzymology. 85. Cambridge, Massachusetts: Academic Press; 1982. p. 20-55.

103. Squire JM. Architecture and function in the muscle sarcomere. COSB. 1997;7(2):247-57.

104. Kreplak L, Bär H, Leterrier JF, Herrmann H, Aebi U. Exploring the mechanical behavior of single intermediate filaments. J Mol Biol. 2005;354(3):569-77.

105. Kremer HaW, Eric W. Isoperimetric Quotient: MathWorld, A Wolfram Web Resource; 2025 [updated 2025.02.15.; cited 2025.05.24.] Available from: https://mathworld.wolfram.com/IsoperimetricQuotient.html.

106. Tordeux C, Fournier J, Galatola P. Analytical characterization of adhering vesicles. Phys Rev E. 2001.

107. Ke Z, Oton J, Qu K, Cortese M, Zila V, McKeane L, et al. Structures and distributions of SARS-CoV-2 spike proteins on intact virions. Nat. 2020;588(7838):498-502.

108. Schaap IA, Eghiaian F, des Georges A, Veigel C. Effect of envelope proteins on the mechanical properties of influenza virus. J Biol Chem. 2012;287(49):41078-88.

109. Won Y. Yang WC, Jaekwon Kim, Kyung W. Park, Ho-Hyun Park, Jingon Joung, Jong-Suk Ro, Han L. Lee, Cheol-Ho Hong, Taeho Im. Applied Numerical Methods Using Matlab. Hoboken, New Jersey: Wiley; 2020. p. 305-74.

110. Kozlov MM, Taraska JW. Generation of nanoscopic membrane curvature for membrane trafficking. Nat Rev Mol Cell Biol. 2023;24(1):63-78.

111. Nečas D, Klapetek P. Gwyddion: An open-source software for SPM data analysis. Cent Eur J Phys. 2011;10.

112. Wang Y, Lu T, Li X, Wang H. Automated image segmentation-assisted flattening of atomic force microscopy images. Beilstein J Nanotechnol. 2018;9:975-85.

113. Software G. Graphpad Prism. v8.0.1. ed: Dotmatics; 2025.

114. Harris CR, Millman KJ, van der Walt SJ, Gommers R, Virtanen P, Cournapeau D, et al. Array programming with NumPy. Nat. 2020;585(7825):357-62.

115. Virtanen P, Gommers R, Oliphant TE, Haberland M, Reddy T, Cournapeau D, et al. SciPy 1.0: fundamental algorithms for scientific computing in Python. Nat Methods. 2020;17(3):261-72.

116. Team TPD. Pandas Python package. v2.2.3 ed: Zenodo; 2024.

117. Hunter JD. Matplotlib: A 2D graphics environment. CiSE. 2007;9(3):90-5.

118. Waskom M, Botvinnik O, Hobson P, Cole JB, Halchenko Y, Hoyer S, et al. seaborn: v0.5.0. v0.5.0 ed: Zenodo; 2014.

119. Taniguchi M, Matsumoto O, Suzuki S, Nishino Y, Okuda A, Taga T, et al. MgATP-induced conformational changes in a single myosin molecule observed by atomic force microscopy: periodicity of substructures in myosin rods. Scanning. 2003;25(5):223-9.

120. Walker M, Trinick J. Electron microscope study of the effect of temperature on the length of the tail of the myosin molecule. J Mol Biol. 1986;192(3):661-7.

121. Kellermayer MSZ, Bustamante C, Granzier HL. Mechanics and structure of titin oligomers explored with atomic force microscopy. BBA Bioenergetics. 2003;1604(2):105-14.

122. Nave R, Fürst DO, Weber K. Visualization of the polarity of isolated titin molecules: a single globular head on a long thin rod as the M band anchoring domain? J Cell Biol. 1989;109(5):2177-87.

123. AL-Khayat HA, Kensler RW, Squire JM, Marston SB, Morris EP. Atomic model of the human cardiac muscle myosin filament. PNAS. 2013;110(1):318-23.

124. Knappeis GG, Carlsen F. The ultrastructure of the M line in skeletal muscle. J Cell Biol. 1968;38(1):202-11.

125. Lange S, Himmel M, Auerbach D, Agarkova I, Hayess K, Fürst DO, et al. Dimerisation of Myomesin: Implications for the Structure of the Sarcomeric M-band. J Mol Biol. 2005;345(2):289-98.

126. Pfuhl M, Pastore A. Tertiary structure of an immunoglobulin-like domain from the giant muscle protein titin: a new member of the I set. Structure. 1995;3(4):391-401.

127. Rief M, Gautel M, Oesterhelt F, Fernandez JM, Gaub HE. Reversible unfolding of individual titin immunoglobulin domains by AFM. Sci. 1997;276(5315):1109-12.

128. Fubini B, Ghiazza M, Fenoglio I. Physico-chemical features of engineered nanoparticles relevant to their toxicity. Nanotoxicology. 2010;4:347-63.

129. Fukuda N, Wu Y, Farman G, Irving TC, Granzier H. Titin-based modulation of active tension and interfilament lattice spacing in skinned rat cardiac muscle. Pflügers Arch. 2005;449(5):449-57.

130. Li Y, Lang P, Linke WA. Titin stiffness modifies the force-generating region of muscle sarcomeres. Sci Rep. 2016;6(1):24492.

131. Millman BM, Irving TC. Filament lattice of frog striated muscle. Radial forces, lattice stability, and filament compression in the A-band of relaxed and rigor muscle. Biophys J. 1988;54(3):437-47.

132. Berkemeier F, Bertz M, Xiao S, Pinotsis N, Wilmanns M, Gräter F, et al. Fast-folding α-helices as reversible strain absorbers in the muscle protein myomesin. PNAS. 2011;108(34):14139-44.

133. Tskhovrebova L, Trinick J. Making Muscle Elastic: The Structural Basis of Myomesin Stretching. PLoS Biol. 2012;10(2):e1001264.

134. Horowits R, Podolsky RJ. The positional stability of thick filaments in activated skeletal muscle depends on sarcomere length: evidence for the role of titin filaments. J Cell Biol. 1987;105(5):2217-23.

135. Labeit S, Kolmerer B. Titins: giant proteins in charge of muscle ultrastructure and elasticity. Sci. 1995;270(5234):293-6.

136. Hsin J, Strümpfer J, Lee EH, Schulten K. Molecular origin of the hierarchical elasticity of titin: simulation, experiment, and theory. Annu Rev Biophys. 2011;40:187-203.

137. Pinotsis N, Chatziefthimiou SD, Berkemeier F, Beuron F, Mavridis IM, Konarev PV, et al. Superhelical Architecture of the Myosin Filament-Linking Protein Myomesin with Unusual Elastic Properties. PLoS Biol. 2012;10(2):e1001261.

138. Trinick J. Titin as a scaffold and spring. Cytoskeleton. Curr Biol. 1996;6(3):258-60.

139. Rahman MM, Williams SJ. Membrane tension may define the deadliest virus infection. Colloid Interface Sci Commun. 2021;40:100338.

140. Mateu MG. Mechanical properties of viruses analyzed by atomic force microscopy: a virological perspective. Virus Res. 2012;168(1-2):1-22.

9. Bibliography

9.1 Publications related to the thesis

1. **Dominik Sziklai**, Judit Sallai, Zsombor Papp, Dalma Kellermayer, Zsolt Mártonfalvi, Pires R. H. & Miklós Kellermayer, *Nanosurgical Manipulation of Titin and Its M-Complex*, Nanomaterials, 2022, 12(2), 178.

2. Miklós Kellermayer, **Dominik Sziklai**, Zsombor Papp, Brennan Decker, Eszter Lakatos & Zsolt Mártonfalvi, *Topology of interaction between titin and myosin thick filaments*, J. Struct. Biol., 2018, Volume 203, Issue 1,

9.2 Unrelated publications

1. Csilla Csányi, **Dominik Sziklai**, Tímea Feller, Jolán Hársfalvi & Miklós Kellermayer, *Cryptic Extensibility in von Willebrand Factor Revealed by Molecular Nanodissection*. Int J Mol Sci. 2024 Jul 2;25(13):7296.

10. Acknowledgements

I would like to express my deepest gratitude to my supervisor, Professor Miklós Kellermayer, for their invaluable guidance, continuous support, and mentorship throughout my PhD journey. I am also sincerely thankful to all my lab members for their collaborative spirit, insightful discussions, and constant encouragement. Their camaraderie and assistance have greatly enriched this experience.